Revealing tissue-specific metabolic crosstalk after a myocardial infarction

Muhammad Arif[1, #], Martina Klevstig[2, #], Rui Benfeitas[3], Stephen Doran[4], Hasan Turkez[5], Mathias Uhlén[1], Maryam Clausen[6], Johannes Wikström[7], Damla Etal[6], Cheng Zhang[1], Malin Levin[2], Adil Mardinoglu[1, 4, *], Jan Boren[2, *]

[1]Science for Life Laboratory, KTH - Royal Institute of Technology, Stockholm, SE-17121, Sweden.

[2]Department of Molecular and Clinical Medicine, University of Gothenburg, The Wallenberg Laboratory, Sahlgrenska University Hospital, Gothenburg, Sweden.

[3]National Bioinformatics Infrastructure Sweden (NBIS), Science for Life Laboratory, Department of Biochemistry and Biophysics, Stockholm University, S-10691 Stockholm, Sweden

[4]Centre for Host-Microbiome Interactions, Faculty of Dentistry, Oral & Craniofacial Sciences, King's College London, London, SE1 9RT, United Kingdom.

[5]Department of Medical Biology, Faculty of Medicine, Atatürk University, Erzurum, 25240, Turkey.

[6]Translational Genomics, BioPharmaceuticals R&D, Discovery Sciences, AstraZeneca, Gothenburg, Sweden.

[7]Bioscience Cardiovascular, Research and Early Development, Cardiovascular, Renal and Metabolism (CVRM), BioPharmaceuticals R&D, AstraZeneca, Gothenburg, Sweden

[#]Contributed equally.

*Corresponding authors: Adil Mardinoglu and Jan Boren

Email: adilm@scilifelab.se; Jan.Boren@wlab.gu.se

Abstract/Summary

Myocardial infarction (MI) promotes a range of systemic effects, many of which are unknown. Here, we investigated the alterations associated with MI progression in heart and other metabolically active tissues (liver, skeletal muscle, and adipose) in a mouse model of MI (induced by ligating the left ascending coronary artery) and sham-operated mice. We performed a genome-wide transcriptomic analysis on tissue samples obtained 6- and 24-hours post MI or sham operation. By generating tissue-specific biological networks, we observed: (1) dysregulation in multiple biological processes (including immune system, mitochondrial dysfunction, fatty-acid beta-oxidation, and RNA and protein processing) across multiple tissues post MI; and (2) tissue-specific dysregulation in biological processes in liver and heart post MI. Finally, we validated our findings in independent MI cohorts, using both bulk and single-cell transcriptomic data. Overall, our integrative analysis highlighted both common and specific biological responses to MI across a range of metabolically active tissues.

Keywords

Systems biology; network analysis; whole-body modelling; cardiovascular disease; Myocardial infarction; multi-tissue; metabolically active tissues; liver; adipose; muscle

Introduction

Cardiovascular disease (CVD) is the leading cause of death worldwide, accounting for more than 17 million deaths globally in 2016 (WHO, 2019). Myocardial infarction (MI) is one of the most common causes of CVD-related death, and is the result of severe coronary artery disease that develops from tapered arteries or chronic blockage of the arteries caused by accumulation of cholesterol or plaque (atherosclerosis). MI has been linked to multiple behavioral risk factors (including unhealthy diet, physical inactivity, excessive use of alcohol, and tobacco consumption) that can lead to significant alterations in metabolism that are responsible for hypertension, obesity, diabetes, and hyperlipidemia. These abnormalities are known as the high-risk factors of MI and CVDs in general.

Systems biology has been used in many studies to reveal the underlying molecular mechanisms of complex human diseases and to answer important biological questions related to the progression, diagnosis and treatment of the diseases. The use of systems biology has aided the discovery of new therapeutic approaches in multiple diseases (Mardinoglu et al., 2017b; Mardinoglu and Nielsen, 2015; Nielsen, 2017) by identifying novel therapeutic agents and repositioning of existing drugs (Turanli et al., 2019). Systems biology has also been employed in the identification of novel biomarkers, characterization of patients and stratification of heterogenous cancer patients (Benfeitas et al., 2019; Bidkhori et al., 2018; Lee et al., 2016). Specifically, integrated networks (INs) (Lee et al., 2016) and co-expression networks (CNs) (Lee et al., 2017) have been proven to be robust methods for revealing the key driver of metabolic abnormalities, discovering new therapy strategies, as well as gaining systematic understanding of diseases (Bakhtiarizadeh et al., 2018; Mukund and Subramaniam, 2017).

Previously, multiple studies in individual tissues have been performed and provided new insights into the underlying mechanisms of diseases (Das et al., 2019; Ounzain et al., 2014; Pedrotty et al., 2012; Williams et al., 2018). However, the crosstalk between different tissues and their dysregulation has not been examined in MI and other CVD-related complications (Priest and Tontonoz, 2019). Here we performed an integrated analysis of heart and other metabolically active tissues (liver, skeletal muscle and adipose tissue) using a mouse model of MI. We used several systems biology approaches to obtain a systematic picture of the

83 metabolic alterations that occur after an MI (**Figure 1A**), and validated our findings in human
84 and mouse datasets.

Results

Differential expression analysis shows a pronounced effect on gene expression 24 h post MI

To study global biological alterations and systemic whole-body effects associated with MI, we obtained heart, liver, skeletal muscle, and white adipose tissue from mice 6 h and 24 h after either an MI (induced by ligating the left ascending coronary artery) or a sham operation (as control). We generated transcriptomics data and identified differentially expressed genes (DEGs) 6 and 24 h post MI and sham operation in all tissues, with the most significant differences occurring after 24 h **(Table S1, Figure 1B)**. Principal component analysis (PCA) showed a close clustering between the control (for both time points) and MI (6 h and 24 h separately) samples for heart tissue but clustering by extraction time points (6 h and 24 h clusters) for the other tissues (**Figure S1**). We present the transcriptional changes associated with MI in **Table S1** and the DEGs (FDR < 5%) using an UpSet plot (Lex et al., 2014) in **Figure 1C**.

All tissues showed a more pronounced effect in terms of the number of DEGs 24 h post MI (**Figure 1C**). As expected, the most affected tissue was the heart (393 DEGs at 6 h, 3318 DEGs at 24 h, and 318 DEGs were the same at both time points). By contrast, 136, 641 and 374 genes were significantly changed in liver, skeletal muscle and adipose tissues 24 h post MI compared to control, respectively. More than 33% of the DEGs that significantly changed in the other tissues also changed in the heart (**Figure 1C**). Interestingly, more than 97% of the shared DEGs between heart and skeletal muscle changed in the same direction, with corresponding numbers of 88% and 64% in adipose and liver, respectively.

Functional analysis reveals widespread mitochondrial, fatty acid, immune, and protein and RNA-related alterations post MI with liver shows contrasting trend

We performed gene-set enrichment analysis (GSEA) with KEGG pathways (**Table S2, Figure 1D**) and gene ontology (GO) biological processes (BPs) (**Table S3, Figure 2A**) to identify altered biological functions and pathways 24 h after an MI. Mitochondrial functions (specifically, mitochondrial translation, respiratory chain and oxidative phosphorylation) were significantly downregulated in the heart, muscle and adipose tissues but not in the liver. Processes related to oxidative stress were upregulated in the heart and skeletal muscle. Fatty acid beta-oxidation was downregulated in the heart and adipose but upregulated in the liver.

Processes and pathways related to immune systems were significantly upregulated in the heart and skeletal muscle but significantly downregulated in liver. Processes associated with protein and RNA processing, ribosome biogenesis and protein targeting endoplasmic reticulum were upregulated in all tissues except liver whereas protein processing in endoplasmic reticulum and RNA transport pathways were upregulated in all tissues.

We also observed that liver was showing opposite trends compared to the other tissues in other important functions, such as fatty acid metabolism and immune response. By checking regulation at the gene level, we observed that only 16 DEGs in liver showed opposite regulation compared to the other tissues whereas 97 out of the 136 DEGs in liver were not DEGs in any other tissues (**Table S4**). Therefore, the differences we observed in liver were mainly due to different DEGs rather than opposite regulation compared to other tissues.

Tissue-specific altered biological functions point to specificity of metabolic and signaling responses to MI

The functional analysis also indicated that several metabolic pathways (including cholesterol, ascorbate and aldarate, linoleic acid, and sphingolipid metabolism pathways) and signaling pathways (including GnRH, FoxO, cAMP and prolactin signaling pathways) were significantly upregulated in heart 6 h after an MI (**Table S2**, **Figure S2A**). We also observed significant down regulation of tryptophan metabolism and upregulation of glycosaminoglycan biosynthesis in heart 24 h after an MI (**Table S2**, **Figure S2A**). Processes related to retinol metabolism were upregulated in heart at both timepoints. Pathways that were previously associated with cardiac hypertrophy and cardiac remodeling (e.g. JAK-STAT, MAPK, estrogen, and TNF signaling pathways, and ECM-receptor interaction) were significantly upregulated in heart 6 and 24 h after an MI (**Figure S1B**).

Our analysis also indicated significant metabolic differences in adipose tissue 24 h after an MI (**Figure S2B**). Fructose and mannose metabolism, glyoxylate and dicarboxylate metabolism, glycolysis/gluconeogenesis, and pentose phosphate pathways, glycine, serine and threonine metabolism and pyrimidine metabolism, as well as endocrine systems (e.g. insulin signaling pathway and regulation of lipolysis in adipocytes) were downregulated in adipose tissue. We observed that the PPAR signaling pathway was upregulated whereas glutathione was downregulated in liver 24 h post-infarction (**Figure S2B**). We found that sphingolipid

metabolism and immune-related pathways were upregulated in skeletal muscle 24 h post-infarction (**Figure S2B**).

Reporter metabolite analyses show significant alterations in fatty acid, amino acid, retinol, and estrogen metabolism post MI

To predict the effect of the transcriptional changes on metabolism, we performed reporter metabolite analyses (**Table S5**) using the gene-to-metabolites mapping from the Mouse Metabolic Reaction database (Mardinoglu et al., 2015); results in each tissue 24 h after MI are shown in **Figure 2B**. In agreement with our analyses above, reporter metabolites related to oxidative phosphorylation, such as *ubiquinol*, *ubiquinone*, *NADH* and *NAD+*, were downregulated in all tissues except liver. Moreover, *linolenoyl-CoA, acetyl CoA,* and several other fatty acyl-CoA-related metabolites were downregulated in heart and adipose tissue but upregulated in liver. We also found that several *5-S-glutathionyl* metabolite forms, known to be related to phenylalanine, tyrosine and tryptophan biosynthesis, were downregulated in heart, liver and skeletal muscle. The same pattern of downregulation was also observed for metabolites related to estrogen metabolism, specifically metabolites related to oestrone and its glutathione conjugate derivative. Moreover, *12-keto-LTB4* and *12-oxo-c-LTB3*, related to leukotriene metabolism, and *hepoxilin A3,* an arachidonic acid, were also found to be downregulated in heart, liver, and skeletal muscle.

The liver showed the highest alteration in reporter metabolites, which is attributed to its role as one of the most metabolically active tissues. We found that several reporter metabolites related to retinol metabolism, namely *retinal*, *retinol*, *retinoate*, and *all-trans-18-hydroxyretinoic acid*, were significantly downregulated only in liver tissue. Retinol metabolism has been previously associated with MI (Lima et al., 2018; Palace et al., 1999).

Network analyses unveil universal and tissue-specific clusters and mechanisms post MI

The use of co-expression network (CN) analyses can assist in elucidating the functional relationships between genes in a specific cell and tissue (Lee et al., 2017). Here, we performed CN analysis to reveal the functional relationship between the DEGs by generating tissue-specific CNs and selected highly connected genes (the top 5% positively correlated genes that fulfilled FDR < 0.05) (**Table 1**). To better define the structure of the networks, we used the Leiden clustering algorithm (Traag et al., 2019) by maximizing the modularity scores

(**Figure 3A-D**) and selected the clusters that include more than 30 genes. Next, we superimposed DEGs 24 h post-infarction onto the network (**Table S1**) and identified the components of the clusters that were affected by an MI. We also used functional analysis with GO BP and KEGG pathways to understand the specific functions associated with each cluster by using the Enrichr algorithm (FDR < 0.05) (Chen et al., 2013; Kuleshov et al., 2016). We summarized the GO BP terms with Revigo (**Table S6**) (Supek et al., 2011) and checked the average clustering coefficient to define the centrality of each cluster (**Table S6**) (Lee et al., 2017). Among the clusters, we identified the key clusters as those with the highest average clustering coefficient, allowing us to identify sets of genes whose time-dependent coordinated changes showed the strongest relationships.

Interestingly, key clusters contained genes with similar functionalities including RNA processing, transports, and RNA metabolic processes in all tissue-specific CNs (**Table S6**). In addition, we found that the majority of the DEGs associated with those clusters were significantly upregulated. These observations strengthen the findings of the functional analysis above (**Figure 2A**) and further highlight how embryonically distinct tissues display similar functional responses to MI, with the most highly connected groups of genes preserved between different tissues (**Table S6**, **Figure 3E**).

Community detection reveals tissue-specific clusters post MI

We investigated the tissue specificity of each cluster by performing enrichment analysis with data from the Mouse Gene Atlas (Su et al., 2004), which involved counting the number of tissue-specific genes.

The heart network showed the highest number of tissue-specific genes in cluster Heart-3 (302 genes). Based on DEG analysis, we found that 522 genes were downregulated and 192 genes were upregulated in the cluster. The enriched GO BP terms in the cluster were mitochondrial transport, protein processing and respiratory chain, cardiac muscle cell action potential, response to muscle stretch, and heart contraction (**Figure 3F**). We observed that the results of the KEGG pathway enrichment analysis were consistent with those obtained from GO BP analysis (**Table S6**).

In the liver network, cluster Liver-2 showed the highest tissue specificity (479 genes). In this cluster, we found that 15 genes were significantly downregulated and 17 genes were significantly upregulated. Based on GO BP enrichment analysis, the genes in this cluster were associated with cholesterol metabolism and homeostasis, lipid transport, glutathione metabolism, lipoprotein metabolism, and glucose 6-phosphate metabolism (**Table S6**). KEGG enrichment analysis also showed that the genes in the cluster were related to retinol, carbohydrate, lipid and amino-acid metabolism (**Table S6**).

The muscle network had two clusters with high tissue specificity: cluster Muscle-4 (276 genes) and Muscle-5 (143 genes). Muscle-4 showed association with GO BP terms such as mitochondrial transport, protein processing and respiratory chain, response to muscle stretch, and muscle contraction (**Table S6**). In contrast, the KEGG pathway in this cluster showed relation to glycolysis/glucogenesis, propanoate metabolism, glyoxylate and dicarboxylate metabolism, and several signaling pathways (e.g. oxytocin, glucagon, cGMP-PKG and HIF-1) (**Table S6**). Muscle-5 was enriched in GO BP terms associated with protein dephosphorylation, muscle contraction and intracellular protein transport (**Table S6**). We also found that insulin, MAPK and Wnt signaling pathways were associated to Muscle-5 from the KEGG enrichment analysis (**Table S6**).

The adipose tissue network showed tissue specificity in cluster Adipose-2 (33 genes), which is associated with GO BP processes including mRNA processing, regulation of mitotic cell cycle phase, ribosome biogenesis, and viral processes (**Table S6**). We observed that the results of the KEGG pathway enrichment analysis were consistent with those obtained from GO BP analysis, with additional associations with multiple signaling and regulatory pathways (**Table S6**).

Tissue-specific clusters show important tissue-specific changes post MI

To understand the specific behavior of each tissue, we further studied the tissue-specific clusters in the CNs (**Figure 4A**). Heart specific cluster, Heart-3, was driven by several central genes including *Pln*, *Pde4b*, and *Atp2a2* (related to regulation of cardiac muscle contraction) and Pdha*1* and *Vdac1* (related to mitochondrial functions). These genes were also found to be significantly differentially expressed in heart 24 hours post MI (**Table S1**). Genes in the heart-specific cluster were related to multiple other processes/pathways, e.g. oxytocin

signaling pathway, and several metabolic pathways (glycogen, inositol phosphate and purine) (**Table S6**).

Mitochondrial dysfunction in the heart leads to disturbance of energy (ATP) production (Kiyuna et al., 2018; Palaniyandi et al., 2010) and, in the presence of oxygen, to accumulation of reactive oxygen species (ROS), which can cause oxidative stress. *Vdac1*, a key gene for regulation of mitochondria function and one of the central genes in the heart-specific cluster (see above), is significantly downregulated in MI (Camara et al., 2017). *Vdac1* is located in the outer mitochondrial membrane and is involved directly in cardioprotection (Schwertz et al., 2007) within the cGMP/PKG pathway (**Figure S3A**). In the same pathway, we also observed down-regulation of the reporter metabolite hydrogen peroxide (**Table S5**), a ROS that is related to cardioprotection (Schwertz et al., 2007; Yada et al., 2006). We also observed downregulation of *Pdha1*, which is known to have a substantial role in both the HIF-1 signaling pathway and the pyruvate metabolism pathway that converts pyruvate to acetyl-CoA in the mitochondria (**Figure S3B**). Acetyl-CoA is used in the TCA cycle to produce NADH and FADH2, which are both needed for ATP production and were downregulated in our reporter metabolite analysis of the heart. Our findings are thus consistent with dysfunctional mitochondria and ATP production in the heart in response to an MI. *Pdha1* has been also been linked to the heart sensitivity during to ischemic stress, where its deficiency can compromise AMP-activated protein kinase activation (Sun et al., 2016).

In skeletal muscle and adipose tissue, we found that central genes in their respective tissue-specific clusters related to fatty acid metabolism and lipid metabolism were significantly altered (**Table S6**, **Figure 5**). In liver-specific cluster, we found that their central genes were related to fatty-acid beta oxidation (*Cyp4a31*, *Cyp4a32*) and glutathione metabolism (*Gstm3*) (**Table S6**, **Figure 5A**). Alterations of fatty acid beta-oxidation and glutathione metabolism have previously been reported in non-alcoholic fatty liver disease, a known risk factor of CVD (Alexander et al., 2019; Mardinoglu et al., 2017a). Moreover, in liver, we also found that retinol metabolism was uniquely related to genes in the liver-specific cluster, mainly driven by four significantly differentially expressed central genes of the clusters, i.e. *Cyp26a1*, *Cyp4a31*, *Cyp4a32*, and *Hsd17b6* (**Table S6**). A previous study showed that mortality from CVD in older individuals was accompanied by impaired liver ability to store retinol (Lima et al., 2018).

Multi-tissue modeling reveals key metabolic pathways affected post MI

To investigate the metabolic responses to MI in and across tissues in the mice, we constructed a multi-tissue genome-scale metabolic model. The model consisted of five tissue-specific genome scale metabolic models, namely heart, liver, skeletal muscle, adipose, and small intestine. The small intestine model (for which we do not have transcriptomic data) was added to include ingestion and conversion of dietary nutrients into chylomicrons, which are directly secreted into blood and transport lipids to other tissues (Mardinoglu et al., 2015). The final mouse multi-tissue model included 19,859 reactions, 13,284 metabolites, 7,116 genes and 41 compartments. We predicted the metabolic fluxes in mice 24 h after an MI or sham operation by integrating the dietary input, tissue-specific resting energy expenditure and transcriptomics data.

The modeling showed that oxygen uptake, carbon dioxide production and the oxidative phosphorylation pathway in heart, adipose and skeletal muscle were decreased in MI mice, in agreement with the downregulation of oxidative phosphorylation we observed in these tissues (**Table S7**). By contrast, liver showed slightly increased oxygen uptake, which might due to the slightly (not statistically significant) upregulated oxidative phosphorylation (**Table S7**). These findings indicate that the changes in oxygen and carbon dioxide fluxes and the oxidative phosphorylation pathway could serve as a positive control for predicting the changes due to MI in the fluxes.

Next, we investigated the tissue-specific metabolic flux changes in the same model (**Table S7**). We found that the pentose phosphate pathway was upregulated in heart 24 hours post MI, consistent with upregulated glucose metabolism after an MI. Elevated glycolysis could allow the heart to rapidly generate energy under stress conditions, and the enhanced pentose phosphate pathway could increase the NADPH level, which could help maintain the level of reduced glutathione in heart (Tran and Wang, 2019). We also found that adipose tissue secreted more ketone bodies, including acetoacetate and butyrate, into plasma; the plasma level of ketone bodies has been reported as a stress marker in acute MI (Miyamoto et al., 1999). Notably, relatively small metabolic changes were found in liver and skeletal muscle, which is probably due to the small number of transcriptomic changes in metabolic pathways in these tissues.

Single-cell analysis highlights cell-type patterns among central genes in a heart-specific cluster

We then questioned whether and how our gene set from both central and heart-specific clusters identified by bulk RNA-seq data would perform at the single cell level. We examined the DEGs from most central and heart-specific cluster genes in an independent single-cell dataset of heart failure in human (Wang et al., 2020). We observed that the majority of the heart-specific genes clustered together in both cardiomyocyte- (CM) and non-CM-enriched data during heart failure, with higher expression levels in CM-enriched data (**Figure S4**). On the other hand, the genes from the most central cluster showed no particular clustering pattern. We also analyzed the clustered tissue-specific genes, and found three distinct groups: group 1, which consisted of genes related to the TCA cycle, glycolysis and HIF-1 signaling pathways; group 2, which consisted of genes with higher expression in all cell types and were related to heart-specific functions and propanoate and pyruvate metabolism; and group 3, which consisted of genes related to cholesterol and lipid metabolism and cGMP-PKG signaling pathways.

Although these gene sets were identified through analysis of bulk RNA-seq data, a clustering analysis through UMAP (McInnes et al., 2018) highlighted clear distinctions between CM- and non-CM-enriched data at the single-cell level (**Figure 6A**). We found that CM-enriched cells (consisting of ~43% smooth muscle cells and ~36% fibroblasts) (**Figure 6B, top left**) were dominated by the mean expression of genes from the heart-specific cluster (**Figure 6C**), with very high expression of genes in groups 1 and 2 (**Figure 6D-E**). By contrast, non-CM cells showed a large heterogeneity in terms of cell type (**Figure 6B, right**). Furthermore, this cluster showed low mean expression of gene groups 1 and 3, and lower mean expression of gene group 2 than did CM-enriched cells (**Figure 6D-F**). Approximately 22% of the non-CM cells were dominated by genes from the most central cluster (**Figure 6C**), whereas 76% of those cells were endothelial cells. Finally, we observed that the central cluster (**Figure 6C orange**) tended to display overall lower expression of gene group 2 (**Figure 6E bottom right**). Altogether, these observations indicate that heart-specific and central clusters tend to display distinct patterns of gene expression and distribution among cell subtypes, both in CM and non-CM-enriched cells.

Validating our findings with publicly available datasets

We validated our observations in heart tissue in two independent cohorts of bulk RNA-seq data from mouse heart (**Table S8**). We filtered both validation cohorts to get and analyzed only 24 hours post-MI data. We found that there were 2169 DEGs in heart 24 h after infarction from our data were validated in at least one of the independent cohort (959 in both) (**Figure 6G)**. We also found that 109 out of the 123 most connected genes in our heart-specific cluster were also significantly differentially expressed in at least one of the independent cohorts (81 in both). By performing functional analysis of the validation cohorts, we found that ~61% of GO BP and 84% of KEGG pathways identified in our analysis of the heart were also present in at least one of the validation cohorts 24 h after infarction (**Figure 6H-I**). In both cohorts, we observed downregulation of mitochondrial functions and fatty acid metabolism processes. We also observed upregulation of processes and pathways related to retinol metabolism and inflammatory response in both validation cohorts.

Identification of driver genes in MI

We observed that *Flnc*, *Lgals3*, *Prkaca* and *Pprc1* showed important response to MI. These genes were 4 of 16 genes that were DEGs in at least three tissues and validated in both validation cohorts (**Table S9**). *Flnc*, *Lgals3* and *Pprc1* were upregulated in heart, skeletal muscle, and adipose, whereas *Prkaca* was downregulated in these three tissues. We further retrieved their neighbors at each tissue specific CNs, showed their regulations from differential expression results, and performed functional analysis in **Table S9**.

Flnc, which encodes filamin-C, was part of heart and skeletal muscle-specific CN cluster and also part of gene group 2 at the single-cell level (**Figure S4**). Its neighbor genes were found to be significantly (FDR < 0.05) associated to several functions, including TCA cycle, pyruvate metabolism, glycolysis pathway, and involved in mitochondrial functions. Specifically, they were related to heart-specific processes in heart, VEGF signaling pathway in muscle, carbohydrate metabolism in adipose, and to MAPK signaling pathway and muscle contraction in heart and muscle.

Lgals3 (encodes galectin-3) and *Prkaca* were among the most central genes in central clusters (**Table S6**). The neighbors of *Lgals3* were significantly related to cell cycle and protein digestion and absorption pathway in all tissues, and to RNA and mRNA related-processes in

muscle and adipose tissue. The neighbors of *Prkaca* were related to insulin signaling pathway in heart and adipose, and several mitochondrial functions in adipose. *Pprc1* was part of most central clusters in heart and adipose tissue CN, and its neighbors were related to ribosomal RNA processing and ribosome biogenesis.

The median expression of these genes at the single-cell level is shown in **Table S9, Figure S5**. We found that all genes were expressed in all cell types in CM and non-CM enriched cells, except *Pprc1*. In CM cells, *Flnc* showed highest median expression in macrophages, whilst *Prkaca* showed highest median expression in fibroblasts. *Lgals3* had similar median expression in all cell types. More heterogeneity was seen in non-CM cells: *Flnc* showed high median expression in macrophages and fibroblasts, whilst *Lgals3* were observed to have high median expression in fibroblasts.

Discussion

CVD has a complex etiology and is responsible for a range of systemic effects, hindering our understanding of its consequences on different tissues. Here, we took advantage of the technological advances in high-throughput RNA-seq and applied integrative network analyses to comprehensively explore the underlying biological effects of MI. Specifically, we generated RNA-seq data from heart, liver, skeletal muscle and adipose tissue obtained from mice 6 and 24 h after an MI or sham operation. We used transcriptomics data analyses (differential expression, functional analysis, and reporter metabolites analysis) to determine the systemic effects of the MI across multiple tissues. Moreover, we performed CN analyses to pinpoint important key and tissue-specific clusters in each tissue, and identified the key genes in each cluster. Finally, we used a whole-body modelling approach to identify the crosstalk between tissues and reveal the global metabolic alterations, before finally validating our findings with publicly available independent MI cohorts.

Based on our analyses, we observed downregulation of heart-specific functions and upregulation of lipid metabolism and inflammatory response in heart, muscle, and adipose tissue after an MI (**Figure 4B**). Liver showed a distinct response with respect to the other three tissues, including downregulation of inflammatory response. We observed that fatty acid metabolism was downregulated in heart and adipose tissue, whereas fatty acid beta-oxidation was upregulated and glutathione metabolism was downregulated in liver. We also observed upregulation of oxidative stress in heart and skeletal muscle. We also observed downregulation of mitochondrial functions in heart, muscle, and adipose tissue. Furthermore, we found upregulation of retinol metabolism in heart and downregulation of retinol metabolites in liver (**Figure 4B**).

We hypothesized that downregulation of fatty acid metabolism from adipose tissue was due to exchange of fatty acids with other tissues (liver and muscle) (**Figure 4B**). We also observed the flow of retinol from liver to heart during MI, consistent with previous reports (Palace et al., 1999). These MI-associated alterations lead to dysfunctional mitochondria and decreased energy production, especially in heart and skeletal muscle.

We further examined our results with single cell RNA-seq data. Although our gene set was extracted from bulk RNA-seq data analysis, it still had a strong presence at the single cell

RNA level, in both CM and NCM cells. We also validated our results with publicly available MI datasets generated in separate independent studies. The validation results strengthened our findings on the altered functions/pathways and the important heart-specific genes after an MI.

Importantly, our analyses of gene clusters highlighted multiple key genes in the response to MI in different tissues. Specifically, we observed that *Flnc*, *Prkaca, Lgals3*, and *Pprc1* showed important responses in heart, skeletal muscle, and adipose tissue. Moreover, *Flnc*, *Lgals3,* and *Prkaca* showed strong presence at the single cell level. *Flnc* is involved in actin cytoskeleton organization in heart and skeletal muscle, and previous studies have shown that this gene has critical role in CVD (Hall et al., 2020; Zhou et al., 2020). Similarly, *Prkaca,* an important metabolic gene, has also been shown to play an important function during CVD (Bers, 2008; Diviani et al., 2011; Turnham and Scott, 2016). *Lgals3*, related to acute inflammation response, has been studied intensively in recent years as a key gene in CVD, and as a potential CVD therapy target (Suthahar et al., 2018; Zhong et al., 2019). Lastly, *Pprc1*, as important regulator of mitochondrial biogenesis, has not been explored for its direct relationship with CVD; however, mitochondrial biogenesis appears to be an important response to CVD (Piantadosi and Suliman, 2012; Ren et al., 2010; Siasos et al., 2018).

In summary, we systematically unveiled the deregulation of biological processes and pathways that resulted from MI in heart, liver, muscle, and adipose tissue by integrating transcriptomic data and the use of biological networks. We also identified the key clusters and central genes using generated tissue-specific CNs. In this study, we demonstrated a strategy to utilize multi-tissue transcriptomic data to identify alteration of biological processes and pathways to systemically explore the effect of a disease.

Limitation of the Study

We recognized several limitations to be noted on this research. First, only transcriptomic data was analyzed in this research, hence the sensitivity might be limited especially for short timepoint, e.g. 6 hours after MI. Second, we focused our analysis in this research only on protein-coding genes. Third, to explore more about the shift in metabolism due to MI, longer timepoints needs to be explored. This opens new opportunities for future research, including analyzing the non-protein-coding gene signatures and longer timepoints.

Author Contribution

MK performed the animal experiments, MA performed the computational analysis and analyzed the clinical data together with RB, SD, HT, MU, MC, JW, DE, CZ, AM, and JB coordinated the generation of the clinical data. MA, MK, AM and JB wrote the paper and all authors were involved in editing the paper.

Acknowledgements

This work was financially supported by the Knut and Alice Wallenberg Foundation, Swedish Research Foundation and Swedish Heart-Lung Foundation.

Conflict of Interest

JW, MC, DE are employees at AstraZeneca. The other authors declare no conflict of interest.

Figure Legends

Figure 1 *(A) Overview of this study (B) Number of differentially expressed genes for each tissue at each time point. Effect of MI shown to be more pronounced after 24 h. (C) UpSet plot to show intersection between differentially expressed genes (FDR < 5%) in different tissues. The plot showed that each tissue has its specific set of genes that were affected by MI. (D) KEGG pathway analysis (FDR < 0.05 in at least 3 tissues) for 24 hours post MI compared to its control for each tissue. We observed that 141 (5 upregulated) and 125 (14 upregulated) pathways are significantly altered in heart 6 and 24 h after infarction, respectively. For other tissues, we found that 24 (9 upregulated), 61 (54 upregulated) and 48 (15 upregulated) pathways are altered in liver, muscle, and adipose, respectively.*

Figure 2 *(A) Functional analysis with GO (FDR < 0.05% in at least 3 tissues) revealed that 944 (919 upregulated) and 1019 (970 upregulation) BPs are significantly altered in heart 6 and 24 h after infarction, respectively. The results also showed 38 (16 upregulated), 376 (357 upregulated) and 193 (116 upregulated) BPs are significantly altered 24 h after infarction in liver, muscle and adipose, respectively. Most tissues show significant alterations in multiple biological processes, including mitochondrial functions, RNA processes, cell adhesion, ribosome and immune systems. The results of this analysis showed alterations concordant with those observed for KEGG pathways. (B) Reporter metabolites analysis shows significant alternation in important metabolites. Our analysis revealed that 169, 324, 118 and 51 reporter metabolites are significantly altered in heart, liver, skeletal muscle and adipose tissues, respectively, at 24 h post-infarction (Table S4)*

Figure 3 *Network analyses. (A) Heart co-expression network clusters with superimposed DEGs 24 h post-infarction (Blue = down-regulated, Red = up-regulated) marked with the cluster numbers. The edges between the clusters were aggregation of the inter-cluster edges (B) Liver. (C) Muscle. (D) Adipose. (E) Intersection of the most central clusters in all tissues shows that the central architecture of the network was conserved in all tissues. We found 4 sub-clusters within the network intersection. Top 10 most connected genes are marked in black. (F) Enriched GO BP in heart-specific cluster generated by Revigo.*

Figure 4 *(A) Similarity of functions in the most central cluster and specific functions of each tissue-specific cluster. (B) Functional analysis for each tissue and hypothesized flow of metabolites*

Figure 5 (*A) Significantly differentially expressed central genes of each tissue-specific cluster to fatty acid metabolism, as one of the most affected metabolic process. (B) Lipid metabolism. Red = upregulated, blue = downregulated.*

Figure 6 *(A-C) UMAP clustering of the single cell RNA-seq data with our gene set based on the CM enrichment, cell types, and network gene cluster type (D-F) colored based on the mean expression of the gene groups (G) DEGs intersection of our data and validation cohort (H) & (I) Intersection of functional analysis results (GO BP and KEGG Pathways) of our data and validation cohort*

514 **Table**

515 *Table 1 Properties of the co-expression network*

Tissue	# of Genes	# of Edges	# of Clusters	Modularity Scores
Heart	8793	1570898	7	0.540179085
Liver	7760	1103589	6	0.577273459
Muscle	8834	1660603	7	0.521239124
Adipose	10790	2636378	8	0.495469439

516

STAR Methods

Induction of MI

10-week-old male C57Bl/6N mice were fasted for 4 h before induction of myocardial infarction. The mice were then anesthetized with isoflurane, orally intubated, and connected to a small-animal ventilator (SAR-830, Geneq, Montreal, Canada) distributing a mixture of oxygen, air and 2–3% isoflurane. ECG electrodes were placed on the extremities, and cardiac rhythm was monitored during surgery. An incision was made between the 4th and 5th ribs to reveal the upper part of the anterior left ventricle (LV) wall and the lower part of the left atrium. Myocardial infarction was induced by ligating the left anterior descending (LAD) coronary artery immediately after the bifurcation of the left coronary artery 1. The efficacy of the procedure was immediately verified by characteristic ECG changes, and akinesis of the LV anterior wall. After verification of the infarction, the lungs were hyperinflated, positive end-expiratory pressure was applied, and the chest was closed. Sham mice were handled identically, but no ligation of the LAD coronary artery was performed (and thus, no ischemia was induced in these mice). The mice received an intraperitoneal injection of 0.1 ml buprenorphine to relieve postoperative pain and were allowed to recover spontaneously after stopping isoflurane administration. Mice were killed with an overdose of isoflurane 6 h or 24 h after occlusion or sham operation. We collected the left ventricle (the whole left ventricle containing mainly infarcted tissue) of the heart, whereas white adipose tissue (WAT) was collected from the abdomen and musculus soleus was taken as the muscle tissue. Mouse hearts and biopsies from the liver, muscle and WAT were snap-frozen in liquid nitrogen and stored at -80°C until analysis. All mice studies were approved by the local animal ethics committee and conform to the guidelines from Directive 2010/63/EU of the European Parliament on the protection of animals used for scientific purposes.

Echocardiography in mice

Echocardiographic examination, using VisualSonics VEVO 2100 system (VisualSonics Inc, Ontario, Canada), which includes an integrated rail system for consistent positioning of the ultrasound probe was performed 6 and 24 h after an MI to determine the size of the MI. We calculated infarct size based on wall motion score index (WMSI) 24 h after myocardial infarction by a 16-segments model on 3 short axis images, as 0 for normal, ½ for reduced wall thickening and excursion in a segment and 1 for no wall thickening and excursion in a segment. WMSI was calculated as the sum of scores divided by the total number of segments.

Hair removal gel was applied to isofluorane-anesthetized (1.2%) mice chest to minimize resistance to ultrasonic beam transmission. The mice were then placed on a heating pad and extremities were connected to an ECG. A 55 MHz linear transducer (MS550D) was used for imaging. An optimal parasternal long axis (LAX) cine loop of >1000 frames/s was acquired using the ECG-gated kilohertz visualization technique. Parasternal short axis cine-loops were acquired at 1, 3, and 5 mm below the mitral annulus. Infarct size was calculated based on wall motion score index 6 and 24 hours after myocardial infarction by a 16-segments model on LAX and 3 short axis images view, as 0 for normal, ½ for reduced wall thickening and excursion in a segment and 1 for no wall thickening and excursion in a segment. The data were evaluated using VevoStrain™ software system (VisualSonics Inc, Ontario, Canada).

RNA extraction and sequencing

Total RNA was isolated from homogenized heart tissue using RNeasy Fibrous Tissue Mini Kit (Qiagen). cDNA was synthesized with the high-capacity cDNA Reverse Transcription Kit (Applied Biosystems) and random primers. mRNA expression of genes of interest was analyzed with TaqMan real-time PCR in a ViiA™ 7 system (Applied Biosystems). RNA sequencing library were prepared with Illumina RNA-Seq with Poly-A selections. Subsequently, the libraries were sequenced on NovaSeq6000 (NovaSeq Control Software 1.6.0/RNA v3.4.4) with a 2x51 setup using 'NovaSeqXp' workflow in 'S1' mode flow cell. The Bcl was converted to FastQ by bcl2fastq_v2.19.1.403 from CASAVA software suite (Sanger/phred33/Illumina 1.8+ quality scale).

RNA-sequencing data analysis

The raw RNA-sequencing results were processed using Kallisto (Bray et al., 2016) with index file generated from the Ensembl mouse reference genome (Release-96) (Zerbino et al., 2017). The output from Kallisto, both estimated count and TPM (Trancript per kilobase million), were subsequently mapped to gene using the mapping file retrieved from Ensembl BioMart website, by filtering only protein coding genes and transcripts. Genes with mean expression less than 1 TPM in each condition were filtered. For data exploration, we used PCA from sklearn package (Pedregosa et al., 2011) in Python 3.7 and used TPM values as the input. Subsequently, we performed differential gene expression analysis using DESeq2 package in R. We utilized the capabilities from DESeq2 to normalize the rounded estimated count data and to correct for confounding factors (such as time). To define a gene as differentially

583 expressed (DEGs), a gene has to fulfill a criterion of FDR < 5%. The results of differential
584 expression analysis were then used for functional analysis.
585
586 We checked the tissue specificity of the DEGs in each tissue with the data from Mouse Gene
587 Atlas (Su et al., 2004). For all the tissue-specific genes, we also checked their human-
588 homolog genes in the human secretome database (Uhlén et al., 2019).
589
590 ***Functional analysis***
591 We performed functional analysis using the R package PIANO (Väremo et al., 2013). As the
592 input, we used the fold changes and p-values from the DESeq2, and also GO BP and KEGG
593 pathways gene-set collections from Enrichr (Chen et al., 2013; Kuleshov et al., 2016), and
594 metabolites from Mouse Metabolic Reaction database (Mardinoglu et al., 2015). To define a
595 process or pathway as significant, we used a cut off of FDR < 5% for the distinct direction of
596 PIANO (both up and down).
597
598 ***Co-expression network generation***
599 We generated the co-expression network by generating gene-gene Spearman correlation ranks
600 within a tissue type, using *spearmanr* function from SciPy (Jones et al., 2001) in Python 3.7.
601 Using the same environment, we performed multiple hypothesis testing using Benjamini-
602 Hochberg method from *statsmodels* (Perktold et al., 2017). Correlation data were filtered with
603 criterion of adjusted p-value < 5%.
604
605 The top 5% of filtered correlation results were then loaded into iGraph module (Csardi and
606 Nepusz, 2006) in Python 3.7 as an unweighted network. To find the subnetworks, we
607 employed the Leiden clustering algorithm (Traag et al., 2019) with *ModularityVertexPartition*
608 method. Each cluster was analyzed by using Enrichr (Chen et al., 2013; Kuleshov et al., 2016)
609 to get the enriched GO BP and KEGG pathways. Criterion FDR < 0.05 were used to find the
610 significantly enriched terms. Clusters with less than 30 genes were discarded, to be able to get
611 significant functional analysis results. Since GO BP was relatively sparse, we used Revigo
612 (Supek et al., 2011) to summarize the GO BP into a higher level. Revigo was further
613 employed to build a GO BP network. Clustering coefficient was calculated based on the
614 average local clustering coefficient function within iGraph.
615

Multi-tissue metabolic modeling

We combined tissue-specific models (of heart, liver, muscle, adipose and small intestine) constructed previously (Mardinoglu et al., 2015) in a multi-tissue model by adding an additional compartment representing the plasma, which allows the exchange of metabolites among different tissues. Blocked reactions that could not carry fluxes (and the unused metabolites and genes linked to these reactions) were removed from the models. In addition, the dietary input reactions and constraints were added to the small intestine model to simulate the food intake (**Table S7**). Specifically, we assumed that the mice weighed 30 g and consumed 4.5 g chow diet per day (15 g/100 g body weight) based on a previous study (Kummitha et al., 2014). We also calculated the tissue-specific resting energy expenditures and set them as mandatory metabolic constraints based on previous studies and resting energy expenditure for other tissues was incorporated by including a mandatory glucose secretion flux out from the system with the lower bound calculated based on ATP (**Table S7**) (Kummitha et al., 2014).

To simulate the metabolic flux distribution in the sham-operated mice, we set the lipid droplet accumulation reaction in adipose tissue (m3_Adipose_LD_pool) as the objective function so that the energy additional to the resting energy expenditure will be stored as fat; we used parsimonious FBA to calculate the flux distribution. To simulate the flux distribution after an MI, we used the previously developed method Relative Metabolic Difference ver. 2 (RMetD2) (Zhang et al., 2019) to integrate transcriptomic data. In brief, RMetD2 calculates the expected fluxes of reactions based on their reference fluxes and fold changes of gene expression, and searches for a flux distribution that is close to the expected fluxes while subject to the model constraints.

Validation of the results

We validated our findings by performing similar steps of RNA sequencing and functional analysis for the publicly available mouse MI datasets GSE104187 and GSE52313 (Ounzain et al., 2014; Williams et al., 2018). Single-cell RNA-seq human data for heart failure was retrieved from GSE109816 (Wang et al., 2020). Hierarchical clustering of the single-cell data was performed with *clustermap* function from *seaborn* module in Python.

Data and code availability

All raw RNA-sequencing data generated from this study can be accessed through accession number GSE153485. Codes used during the analysis are available on https://github.com/sysmedicine/ArifEtAll_2020_MultiTissueMI

Supplementary Tables

Table S1 *Differential Expression Analysis Results*

Table S2 *KEGG Pathways*

Table S3 *Gene Ontology Biological Processes*

Table S4 *DEG comparison between Liver and other tissues*

Table S5 *Reporter Metabolite Analysis*

Table S6 *Enrichment Analyses of Clusters, Clusters properties*

Table S7 *Food Intake, Energy Expenditure, and Flux Balance Analysis (FBA) of Whole-Body Modeling*

Table S8 *Validation Result (Differential Expression and Functional Analysis)*

Table S9 *Detailed Information of 16 Key Genes that are DEGs in at least 3 tissues, Neighbors and Functional Analysis Results of The Neighbors of 4 key genes, and mean expression of 4 key genes in each cell-type in the scRNA data.*

References

Alexander, M., Loomis, A.K., van der Lei, J., Duarte-Salles, T., Prieto-Alhambra, D., Ansell, D., Pasqua, A., Lapi, F., Rijnbeek, P., and Mosseveld, M. (2019). Non-alcoholic fatty liver disease and risk of incident acute myocardial infarction and stroke: findings from matched cohort study of 18 million European adults. bmj *367*, l5367.

Bakhtiarizadeh, M.R., Hosseinpour, B., Shahhoseini, M., Korte, A., and Gifani, P. (2018). Weighted Gene Co-expression Network Analysis of Endometriosis and Identification of Functional Modules Associated With Its Main Hallmarks. Frontiers in Genetics *9*.

Benfeitas, R., Bidkhori, G., Mukhopadhyay, B., Klevstig, M., Arif, M., Zhang, C., Lee, S., Cinar, R., Nielsen, J., and Uhlen, M. (2019). Characterization of heterogeneous redox responses in hepatocellular carcinoma patients using network analysis. EBioMedicine *40*, 471-487.

Bers, D.M. (2008). Calcium cycling and signaling in cardiac myocytes. Annu Rev Physiol *70*, 23-49.

Bidkhori, G., Benfeitas, R., Klevstig, M., Zhang, C., Nielsen, J., Uhlen, M., Boren, J., and Mardinoglu, A. (2018). Metabolic network-based stratification of hepatocellular carcinoma reveals three distinct tumor subtypes. Proceedings of the National Academy of Sciences *115*, E11874-E11883.

Bray, N.L., Pimentel, H., Melsted, P., and Pachter, L. (2016). Near-optimal probabilistic RNA-seq quantification. Nature biotechnology *34*, 525.

Camara, A.K., Zhou, Y., Wen, P.-C., Tajkhorshid, E., and Kwok, W.-M. (2017). Mitochondrial VDAC1: a key gatekeeper as potential therapeutic target. Frontiers in physiology *8*, 460.

Chen, E.Y., Tan, C.M., Kou, Y., Duan, Q., Wang, Z., Meirelles, G.V., Clark, N.R., and Ma'ayan, A. (2013). Enrichr: interactive and collaborative HTML5 gene list enrichment analysis tool. BMC Bioinformatics *14*, 128.

Csardi, G., and Nepusz, T. (2006). The igraph software package for complex network research. InterJournal, Complex Systems *1695*, 1-9.

Das, S., Frisk, C., Eriksson, M.J., Walentinsson, A., Corbascio, M., Hage, C., Kumar, C., Asp, M., Lundeberg, J., and Maret, E. (2019). Transcriptomics of cardiac biopsies reveals differences in patients with or without diagnostic parameters for heart failure with preserved ejection fraction. Scientific reports *9*, 3179.

Diviani, D., Dodge-Kafka, K.L., Li, J., and Kapiloff, M.S. (2011). A-kinase anchoring proteins: scaffolding proteins in the heart. American Journal of Physiology-Heart and Circulatory Physiology *301*, H1742-H1753.

Hall, C.L., Gurha, P., Sabater-Molina, M., Asimaki, A., Futema, M., Lovering, R.C., Suárez, M.P., Aguilera, B., Molina, P., and Zorio, E. (2020). RNA sequencing-based transcriptome profiling of cardiac tissue implicates novel putative disease mechanisms in FLNC-associated arrhythmogenic cardiomyopathy. International journal of cardiology *302*, 124-130.

Jones, E., Oliphant, T., and Peterson, P. (2001). SciPy: Open source scientific tools for Python.

Kiyuna, L.A., e Albuquerque, R.P., Chen, C.-H., Mochly-Rosen, D., and Ferreira, J.C.B. (2018). Targeting mitochondrial dysfunction and oxidative stress in heart failure: challenges and opportunities. Free Radical Biology and Medicine *129*, 155-168.

Kuleshov, M.V., Jones, M.R., Rouillard, A.D., Fernandez, N.F., Duan, Q., Wang, Z., Koplev, S., Jenkins, S.L., Jagodnik, K.M., Lachmann, A., *et al.* (2016). Enrichr: a comprehensive gene set enrichment analysis web server 2016 update. Nucleic Acids Research *44*, W90-W97.

Kummitha, C.M., Kalhan, S.C., Saidel, G.M., and Lai, N. (2014). Relating tissue/organ energy expenditure to metabolic fluxes in mouse and human: experimental data integrated with mathematical modeling. Physiological reports *2*.

Lee, S., Zhang, C., Kilicarslan, M., Piening, B.D., Bjornson, E., Hallström, B.M., Groen, A.K., Ferrannini, E., Laakso, M., and Snyder, M. (2016). Integrated network analysis reveals an association between plasma mannose levels and insulin resistance. Cell metabolism *24*, 172-184.

Lee, S., Zhang, C., Liu, Z., Klevstig, M., Mukhopadhyay, B., Bergentall, M., Cinar, R., Ståhlman, M., Sikanic, N., and Park, J.K. (2017). Network analyses identify liver□specific targets for treating liver diseases. Molecular systems biology *13*.

Lex, A., Gehlenborg, N., Strobelt, H., Vuillemot, R., and Pfister, H. (2014). UpSet: visualization of intersecting sets. IEEE transactions on visualization and computer graphics *20*, 1983-1992.

Lima, I., Peres, W., Cruz, S., and Ramalho, A. (2018). Association of Ischemic Cardiovascular Disease with Inadequacy of Liver Store of Retinol in Elderly Individuals. Oxidative medicine and cellular longevity *2018*.

Mardinoglu, A., Bjornson, E., Zhang, C., Klevstig, M., Söderlund, S., Ståhlman, M., Adiels, M., Hakkarainen, A., Lundbom, N., and Kilicarslan, M. (2017a). Personal model□assisted identification of NAD+ and glutathione metabolism as intervention target in NAFLD. Molecular systems biology *13*.

Mardinoglu, A., Boren, J., Smith, U., Uhlen, M., and Nielsen, J. (2017b). The employment of systems biology in gastroenterology and hepatology. Nat Rev Gastroenterol Hepatol.

Mardinoglu, A., and Nielsen, J. (2015). New paradigms for metabolic modeling of human cells. Current Opinion in Biotechnology *34*, 91-97.

Mardinoglu, A., Shoaie, S., Bergentall, M., Ghaffari, P., Zhang, C., Larsson, E., Bäckhed, F., and Nielsen, J. (2015). The gut microbiota modulates host amino acid and glutathione metabolism in mice. Molecular Systems Biology *11*, 834.

McInnes, L., Healy, J., and Melville, J. (2018). Umap: Uniform manifold approximation and projection for dimension reduction. arXiv preprint arXiv:180203426.

Miyamoto, T., Katayama, Y., and Harano, Y. (1999). Blood ketone body as a stress marker in acute myocardial infarction. Nihon Kyukyu Igakukai Zasshi *10*, 621-622.

Mukund, K., and Subramaniam, S. (2017). Co-expression network approach reveals functional similarities among diseases affecting human skeletal muscle. Frontiers in physiology *8*, 980.

Nielsen, J. (2017). Systems biology of metabolism: a driver for developing personalized and precision medicine. Cell metabolism *25*, 572-579.

Ounzain, S., Micheletti, R., Beckmann, T., Schroen, B., Alexanian, M., Pezzuto, I., Crippa, S., Nemir, M., Sarre, A., and Johnson, R. (2014). Genome-wide profiling of the cardiac transcriptome after myocardial infarction identifies novel heart-specific long non-coding RNAs. European heart journal *36*, 353-368.

753 Palace, V.P., Hill, M.F., Khaper, N., and Singal, P.K. (1999). Metabolism of vitamin A in the
754 heart increases after a myocardial infarction. Free Radical Biology and Medicine *26*, 1501-
755 1507.

756 Palaniyandi, S.S., Qi, X., Yogalingam, G., Ferreira, J.C.B., and Mochly-Rosen, D. (2010).
757 Regulation of mitochondrial processes: a target for heart failure. Drug Discovery Today:
758 Disease Mechanisms *7*, e95-e102.

759 Pedregosa, F., Varoquaux, G., Gramfort, A., Michel, V., Thirion, B., Grisel, O., Blondel, M.,
760 Prettenhofer, P., Weiss, R., and Dubourg, V. (2011). Scikit-learn: Machine learning in
761 Python. Journal of machine learning research *12*, 2825-2830.

762 Pedrotty, D.M., Morley, M.P., and Cappola, T.P. (2012). Transcriptomic biomarkers of
763 cardiovascular disease. Progress in cardiovascular diseases *55*, 64-69.

764 Perktold, J., Seabold, S., and Taylor, J. (2017). Statsmodels: Statistics in python (Oct).

765 Piantadosi, C.A., and Suliman, H.B. (2012). Transcriptional control of mitochondrial
766 biogenesis and its interface with inflammatory processes. Biochimica et Biophysica Acta
767 (BBA)-General Subjects *1820*, 532-541.

768 Priest, C., and Tontonoz, P. (2019). Inter-organ cross-talk in metabolic syndrome. Nature
769 Metabolism.

770 Ren, J., Pulakat, L., Whaley-Connell, A., and Sowers, J.R. (2010). Mitochondrial biogenesis
771 in the metabolic syndrome and cardiovascular disease. Journal of molecular medicine *88*,
772 993-1001.

773 Schwertz, H., Carter, J.M., Abdudureheman, M., Russ, M., Buerke, U., Schlitt, A., Müller-
774 Werdan, U., Prondzinsky, R., Werdan, K., and Buerke, M. (2007). Myocardial
775 ischemia/reperfusion causes VDAC phosphorylation which is reduced by cardioprotection
776 with a p38 MAP kinase inhibitor. PROTEOMICS *7*, 4579-4588.

777 Siasos, G., Tsigkou, V., Kosmopoulos, M., Theodosiadis, D., Simantiris, S., Tagkou, N.M.,
778 Tsimpiktsioglou, A., Stampouloglou, P.K., Oikonomou, E., and Mourouzis, K. (2018).
779 Mitochondria and cardiovascular diseases—from pathophysiology to treatment. Annals of
780 translational medicine *6*.

781 Su, A.I., Wiltshire, T., Batalov, S., Lapp, H., Ching, K.A., Block, D., Zhang, J., Soden, R.,
782 Hayakawa, M., Kreiman, G., *et al.* (2004). A gene atlas of the mouse and human protein-
783 encoding transcriptomes. Proceedings of the National Academy of Sciences of the United
784 States of America *101*, 6062-6067.

785 Sun, W., Quan, N., Wang, L., Yang, H., Chu, D., Liu, Q., Zhao, X., Leng, J., and Li, J.
786 (2016). Cardiac-specific deletion of the Pdha1 gene sensitizes heart to toxicological actions of
787 ischemic stress. Toxicological Sciences *151*, 193-203.

788 Supek, F., Bošnjak, M., Škunca, N., and Šmuc, T. (2011). REVIGO summarizes and
789 visualizes long lists of gene ontology terms. PloS one *6*, e21800.

790 Suthahar, N., Meijers, W.C., Silljé, H.H., Ho, J.E., Liu, F.-T., and de Boer, R.A. (2018).
791 Galectin-3 activation and inhibition in heart failure and cardiovascular disease: an update.
792 Theranostics *8*, 593.

793 Traag, V.A., Waltman, L., and van Eck, N.J. (2019). From Louvain to Leiden: guaranteeing
794 well-connected communities. Scientific reports *9*.

795 Tran, D.H., and Wang, Z.V. (2019). Glucose Metabolism in Cardiac Hypertrophy and Heart
796 Failure. Journal of the American Heart Association *8*, e012673.

797 Turanli, B., Zhang, C., Kim, W., Benfeitas, R., Uhlen, M., Arga, K.Y., and Mardinoglu, A.
798 (2019). Discovery of therapeutic agents for prostate cancer using genome-scale metabolic
799 modeling and drug repositioning. EBioMedicine *42*, 386-396.

800 Turnham, R.E., and Scott, J.D. (2016). Protein kinase A catalytic subunit isoform PRKACA;
801 History, function and physiology. Gene *577*, 101-108.

802 Uhlén, M., Karlsson, M.J., Hober, A., Svensson, A.-S., Scheffel, J., Kotol, D., Zhong, W.,
803 Tebani, A., Strandberg, L., Edfors, F., *et al.* (2019). The human secretome. Science Signaling
804 *12*, eaaz0274.

805 Väremo, L., Nielsen, J., and Nookaew, I. (2013). Enriching the gene set analysis of genome-
806 wide data by incorporating directionality of gene expression and combining statistical
807 hypotheses and methods. Nucleic Acids Research *41*, 4378-4391.

808 Wang, L., Yu, P., Zhou, B., Song, J., Li, Z., Zhang, M., Guo, G., Wang, Y., Chen, X., and
809 Han, L. (2020). Single-cell reconstruction of the adult human heart during heart failure and
810 recovery reveals the cellular landscape underlying cardiac function. Nature Cell Biology *22*,
811 108-119.

812 WHO (2019). Cardiovascular diseases (CVDs) Fact sheets.

813 Williams, A.L., Khadka, V., Tang, M., Avelar, A., Schunke, K.J., Menor, M., and Shohet,
814 R.V. (2018). HIF1 mediates a switch in pyruvate kinase isoforms after myocardial infarction.
815 Physiological genomics *50*, 479-494.

816 Yada, T., Shimokawa, H., Hiramatsu, O., Haruna, Y., Morita, Y., Kashihara, N., Shinozaki,
817 Y., Mori, H., Goto, M., and Ogasawara, Y. (2006). Cardioprotective role of endogenous
818 hydrogen peroxide during ischemia-reperfusion injury in canine coronary microcirculation in
819 vivo. American Journal of Physiology-Heart and Circulatory Physiology *291*, H1138-H1146.

820 Zerbino, D.R., Achuthan, P., Akanni, W., Amode, M R., Barrell, D., Bhai, J., Billis, K.,
821 Cummins, C., Gall, A., Girón, C.G., *et al.* (2017). Ensembl 2018. Nucleic Acids Research *46*,
822 D754-D761.

823 Zhang, C., Lee, S., Bidkhori, G., Benfeitas, R., Lovric, A., Chen, S., Uhlen, M., Nielsen, J.,
824 and Mardinoglu, A. (2019). RMetD2: a tool for integration of relative transcriptomics data
825 into Genome-scale metabolic models. BioRxiv, 663096.

826 Zhong, X., Qian, X., Chen, G., and Song, X. (2019). The role of galectin□3 in heart failure
827 and cardiovascular disease. Clinical and Experimental Pharmacology and Physiology *46*, 197-
828 203.

829 Zhou, Y., Chen, Z.e., Zhang, L., Zhu, M., Tan, C., Zhou, X., Evans, S.M., Fang, X., Feng, W.,
830 and Chen, J. (2020). Loss of Filamin C Is Catastrophic for Heart Function. Circulation *141*,
831 869-871.

832

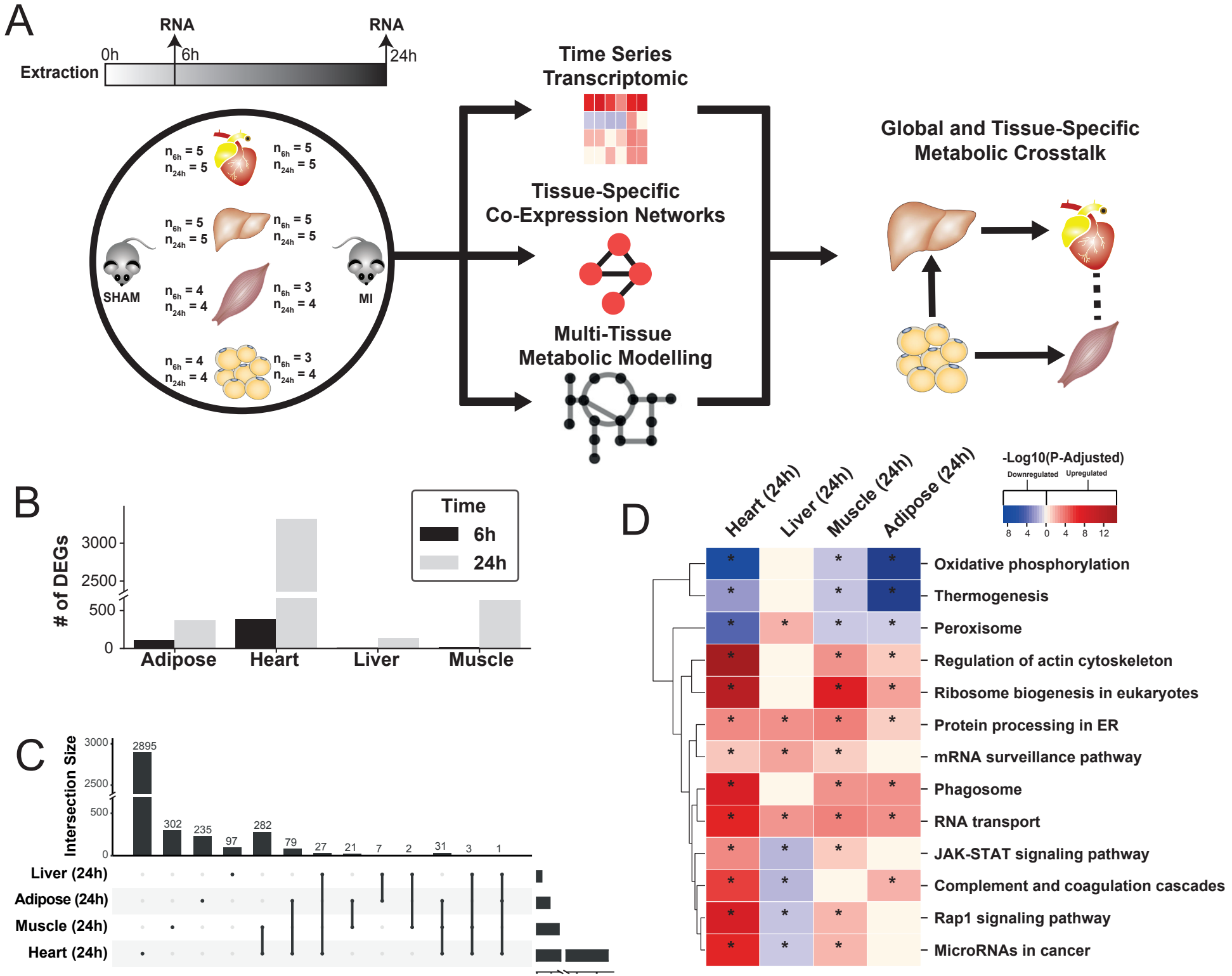
A
RNA
RNA
0h
6h
24h
Extraction
SHAM
MI
Time Series Transcriptomic
Tissue-Specific Co-Expression Networks
Multi-Tissue Metabolic Modelling
Global and Tissue-Specific Metabolic Crosstalk
B
# of DEGs
Time
6h
24h
Adipose
Heart
Liver
Muscle
C
Intersection Size
2895
302
235
97
282
79
27
21
7
2
31
3
1
Liver (24h)
Adipose (24h)
Muscle (24h)
Heart (24h)
D
Heart (24h)
Liver (24h)
Muscle (24h)
Adipose (24h)
-Log10(P-Adjusted)
Downregulated
Upregulated
Oxidative phosphorylation
Thermogenesis
Peroxisome
Regulation of actin cytoskeleton
Ribosome biogenesis in eukaryotes
Protein processing in ER
mRNA surveillance pathway
Phagosome
RNA transport
JAK-STAT signaling pathway
Complement and coagulation cascades
Rap1 signaling pathway
MicroRNAs in cancer

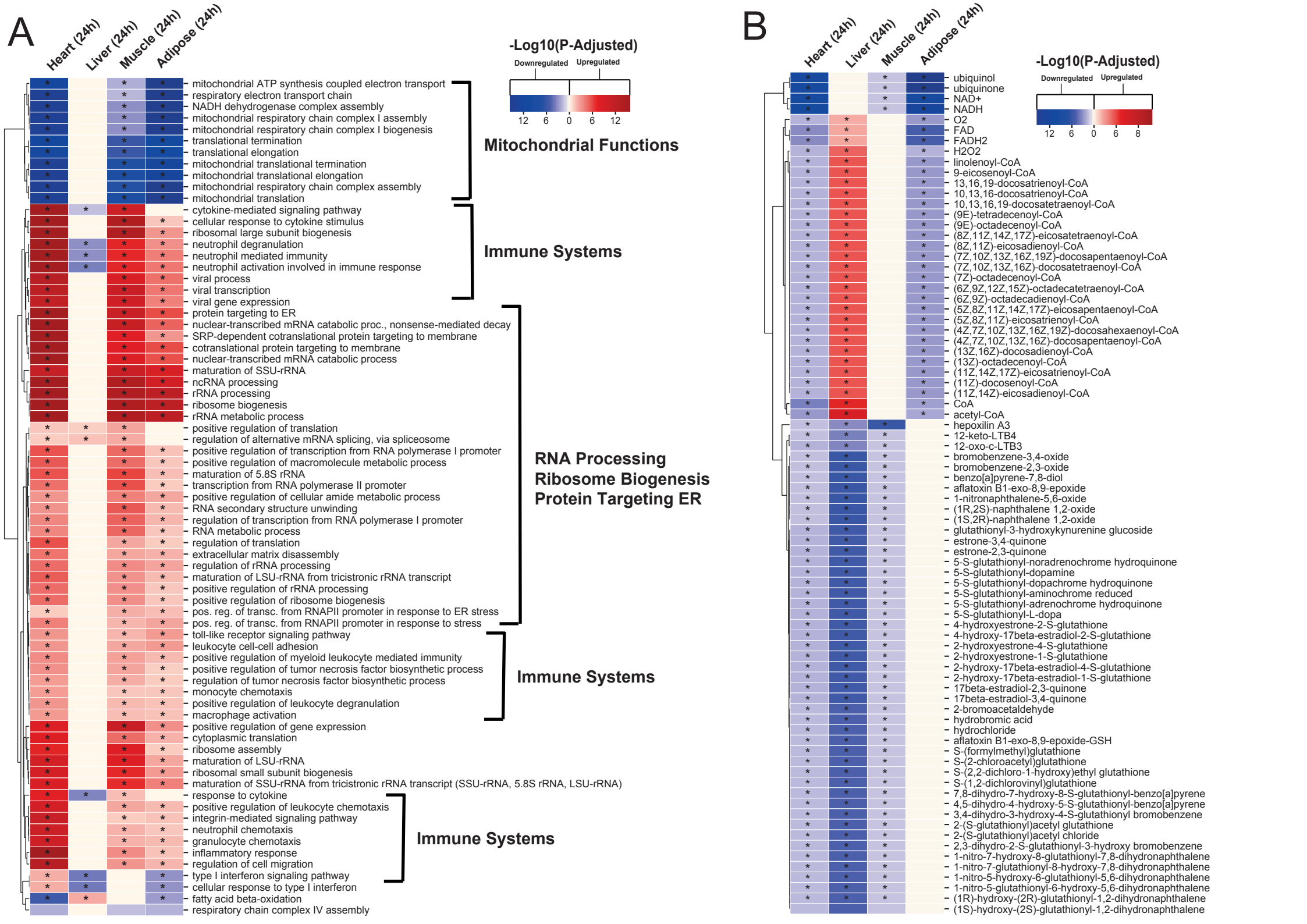
A
Heart (24h)
Liver (24h)
Muscle (24h)
Adipose (24h)
-Log10(P-Adjusted)
Downregulated
Upregulated
12 6 0 6 12
mitochondrial ATP synthesis coupled electron transport
respiratory electron transport chain
NADH dehydrogenase complex assembly
mitochondrial respiratory chain complex I assembly
mitochondrial respiratory chain complex I biogenesis
translational termination
translational elongation
mitochondrial translational termination
mitochondrial translational elongation
mitochondrial respiratory chain complex assembly
mitochondrial translation
Mitochondrial Functions
cytokine-mediated signaling pathway
cellular response to cytokine stimulus
ribosomal large subunit biogenesis
neutrophil degranulation
neutrophil mediated immunity
neutrophil activation involved in immune response
viral process
viral transcription
viral gene expression
Immune Systems
protein targeting to ER
nuclear-transcribed mRNA catabolic proc., nonsense-mediated decay
SRP-dependent cotranslational protein targeting to membrane
cotranslational protein targeting to membrane
nuclear-transcribed mRNA catabolic process
maturation of SSU-rRNA
ncRNA processing
rRNA processing
ribosome biogenesis
rRNA metabolic process
positive regulation of translation
regulation of alternative mRNA splicing, via spliceosome
positive regulation of transcription from RNA polymerase I promoter
positive regulation of macromolecule metabolic process
maturation of 5.8S rRNA
transcription from RNA polymerase II promoter
positive regulation of cellular amide metabolic process
RNA secondary structure unwinding
regulation of transcription from RNA polymerase I promoter
RNA metabolic process
regulation of translation
extracellular matrix disassembly
regulation of rRNA processing
maturation of LSU-rRNA from tricistronic rRNA transcript
positive regulation of rRNA processing
positive regulation of ribosome biogenesis
pos. reg. of transc. from RNAPII promoter in response to ER stress
pos. reg. of transc. from RNAPII promoter in response to stress
RNA Processing
Ribosome Biogenesis
Protein Targeting ER
toll-like receptor signaling pathway
leukocyte cell-cell adhesion
positive regulation of myeloid leukocyte mediated immunity
positive regulation of tumor necrosis factor biosynthetic process
regulation of tumor necrosis factor biosynthetic process
monocyte chemotaxis
positive regulation of leukocyte degranulation
macrophage activation
Immune Systems
positive regulation of gene expression
cytoplasmic translation
ribosome assembly
maturation of LSU-rRNA
ribosomal small subunit biogenesis
maturation of SSU-rRNA from tricistronic rRNA transcript (SSU-rRNA, 5.8S rRNA, LSU-rRNA)
response to cytokine
positive regulation of leukocyte chemotaxis
integrin-mediated signaling pathway
neutrophil chemotaxis
granulocyte chemotaxis
inflammatory response
regulation of cell migration
Immune Systems
type I interferon signaling pathway
cellular response to type I interferon
fatty acid beta-oxidation
respiratory chain complex IV assembly
B
Heart (24h)
Liver (24h)
Muscle (24h)
Adipose (24h)
-Log10(P-Adjusted)
Downregulated
Upregulated
12 6 0 6 8
ubiquinol
ubiquinone
NAD+
NADH
O2
FAD
FADH2
H2O2
linolenoyl-CoA
9-eicosenoyl-CoA
13,16,19-docosatrienoyl-CoA
10,13,16-docosatrienoyl-CoA
10,13,16,19-docosatetraenoyl-CoA
(9E)-tetradecenoyl-CoA
(9E)-octadecenoyl-CoA
(8Z,11Z,14Z,17Z)-eicosatetraenoyl-CoA
(8Z,11Z)-eicosadienoyl-CoA
(7Z,10Z,13Z,16Z,19Z)-docosapentaenoyl-CoA
(7Z,10Z,13Z,16Z)-docosatetraenoyl-CoA
(7Z)-octadecenoyl-CoA
(6Z,9Z,12Z,15Z)-octadecatetraenoyl-CoA
(6Z,9Z)-octadecadienoyl-CoA
(5Z,8Z,11Z,14Z,17Z)-eicosapentaenoyl-CoA
(5Z,8Z,11Z)-eicosatrienoyl-CoA
(4Z,7Z,10Z,13Z,16Z,19Z)-docosahexaenoyl-CoA
(4Z,7Z,10Z,13Z,16Z)-docosapentaenoyl-CoA
(13Z,16Z)-docosadienoyl-CoA
(13Z)-octadecenoyl-CoA
(11Z,14Z,17Z)-eicosatrienoyl-CoA
(11Z)-docosenoyl-CoA
(11Z,14Z)-eicosadienoyl-CoA
CoA
acetyl-CoA
hepoxilin A3
12-keto-LTB4
12-oxo-c-LTB3
bromobenzene-3,4-oxide
bromobenzene-2,3-oxide
benzo[a]pyrene-7,8-diol
aflatoxin B1-exo-8,9-epoxide
1-nitronaphthalene-5,6-oxide
(1R,2S)-naphthalene 1,2-oxide
(1S,2R)-naphthalene 1,2-oxide
glutathionyl-3-hydroxykynurenine glucoside
estrone-3,4-quinone
estrone-2,3-quinone
5-S-glutathionyl-noradrenochrome hydroquinone
5-S-glutathionyl-dopamine
5-S-glutathionyl-dopachrome hydroquinone
5-S-glutathionyl-aminochrome reduced
5-S-glutathionyl-adrenochrome hydroquinone
5-S-glutathionyl-L-dopa
4-hydroxyestrone-2-S-glutathione
4-hydroxy-17beta-estradiol-2-S-glutathione
2-hydroxyestrone-4-S-glutathione
2-hydroxyestrone-1-S-glutathione
2-hydroxy-17beta-estradiol-4-S-glutathione
2-hydroxy-17beta-estradiol-1-S-glutathione
17beta-estradiol-2,3-quinone
17beta-estradiol-3,4-quinone
2-bromoacetaldehyde
hydrobromic acid
hydrochloride
aflatoxin B1-exo-8,9-epoxide-GSH
S-(formylmethyl)glutathione
S-(2-chloroacetyl)glutathione
S-(2,2-dichloro-1-hydroxy)ethyl glutathione
S-(1,2-dichlorovinyl)glutathione
7,8-dihydro-7-hydroxy-8-S-glutathionyl-benzo[a]pyrene
4,5-dihydro-4-hydroxy-5-S-glutathionyl-benzo[a]pyrene
3,4-dihydro-3-hydroxy-4-S-glutathionyl bromobenzene
2-(S-glutathionyl)acetyl glutathione
2-(S-glutathionyl)acetyl chloride
2,3-dihydro-2-S-glutathionyl-3-hydroxy bromobenzene
1-nitro-7-hydroxy-8-glutathionyl-7,8-dihydronaphthalene
1-nitro-7-glutathionyl-8-hydroxy-7,8-dihydronaphthalene
1-nitro-5-hydroxy-6-glutathionyl-5,6-dihydronaphthalene
1-nitro-5-glutathionyl-6-hydroxy-5,6-dihydronaphthalene
(1R)-hydroxy-(2R)-glutathionyl-1,2-dihydronaphthalene
(1S)-hydroxy-(2S)-glutathionyl-1,2-dihydronaphthalene

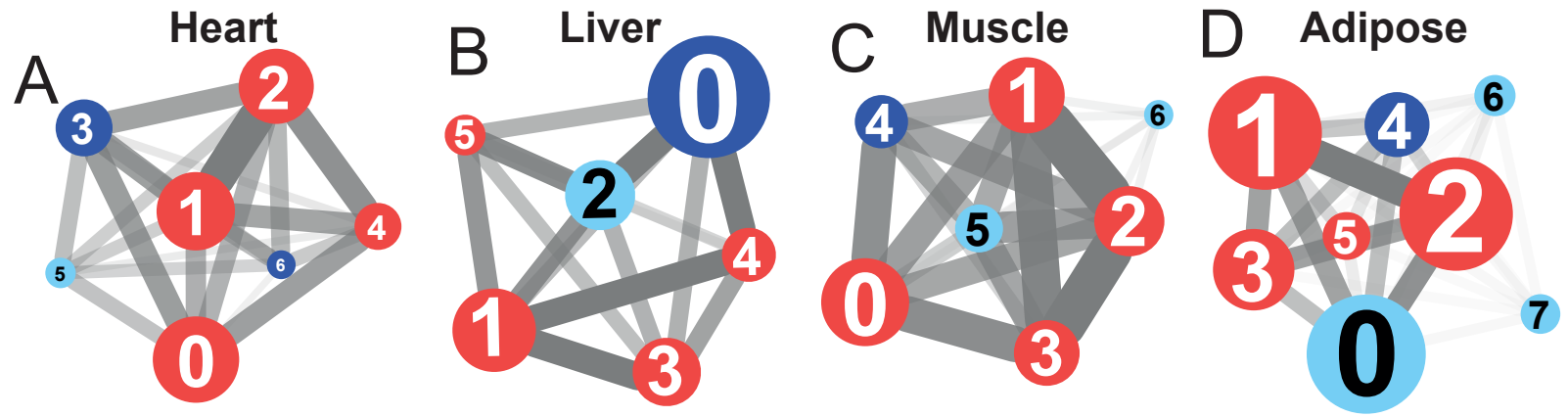
A
Heart
B
Liver
C
Muscle
D
Adipose

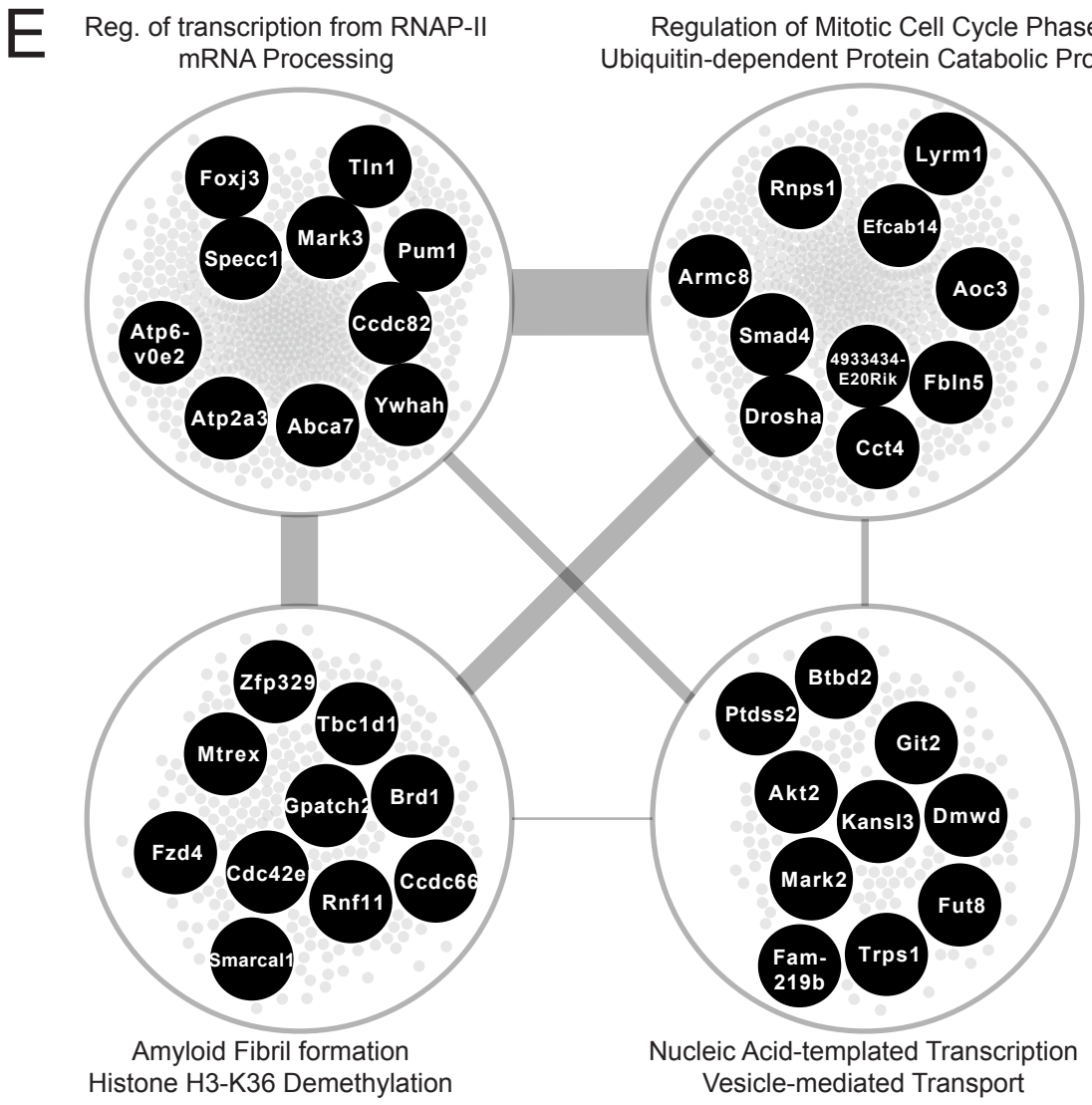
E
Reg. of transcription from RNAP-II
mRNA Processing
Regulation of Mitotic Cell Cycle Phase
Ubiquitin-dependent Protein Catabolic Process
Foxj3
Tln1
Specc1
Mark3
Pum1
Atp6-
v0e2
Ccdc82
Atp2a3
Abca7
Ywhah
Rnps1
Lyrm1
Efcab14
Armc8
Aoc3
Smad4
4933434-
E20Rik
Fbln5
Drosha
Cct4
Zfp329
Tbc1d1
Mtrex
Gpatch2
Brd1
Fzd4
Cdc42e
Rnf11
Ccdc66
Smarcal1
Btbd2
Ptdss2
Git2
Akt2
Kansl3
Dmwd
Mark2
Fut8
Fam-
219b
Trps1
Amyloid Fibril formation
Histone H3-K36 Demethylation
Nucleic Acid-templated Transcription
Vesicle-mediated Transport

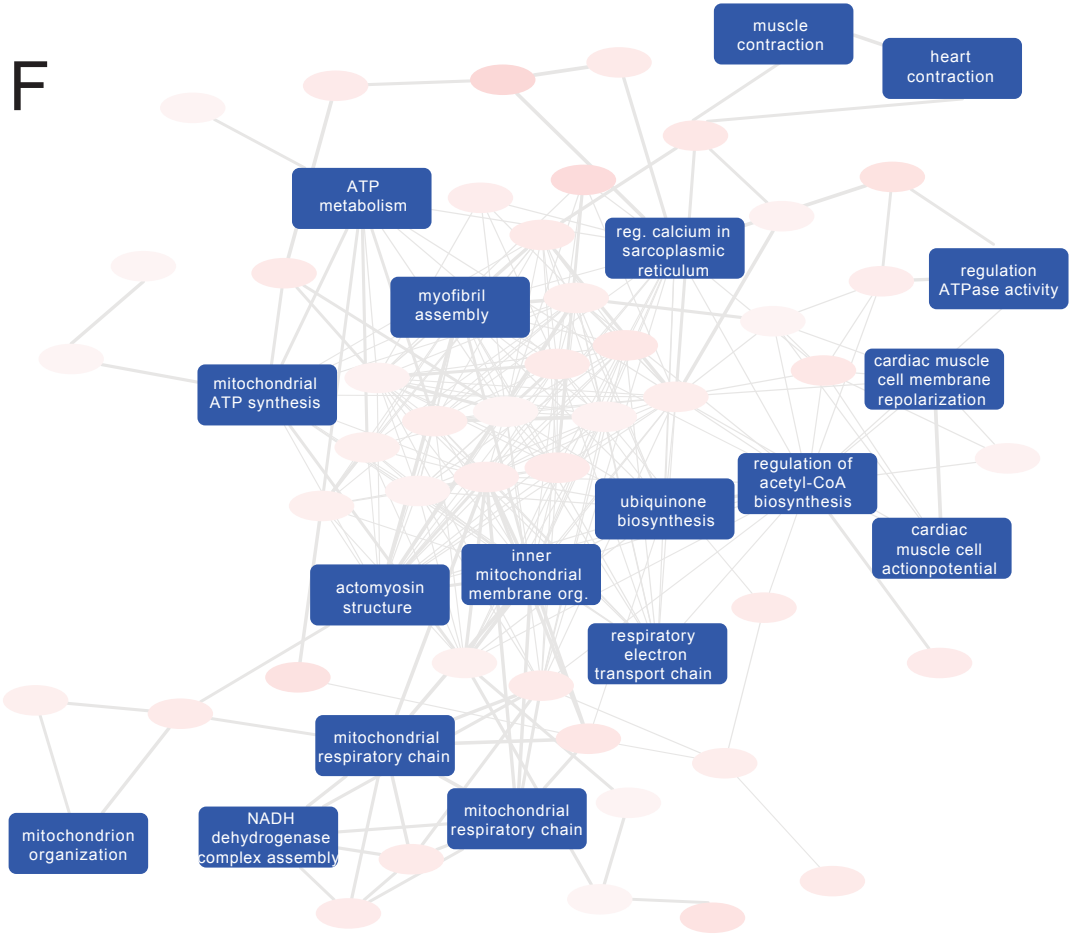
F
muscle
contraction
heart
contraction
ATP
metabolism
reg. calcium in
sarcoplasmic
reticulum
regulation
ATPase activity
myofibril
assembly
mitochondrial
ATP synthesis
cardiac muscle
cell membrane
repolarization
regulation of
acetyl-CoA
biosynthesis
ubiquinone
biosynthesis
cardiac
muscle cell
actionpotential
inner
mitochondrial
membrane org.
actomyosin
structure
respiratory
electron
transport chain
mitochondrial
respiratory chain
mitochondrion
organization
NADH
dehydrogenase
complex assembly
mitochondrial
respiratory chain

A

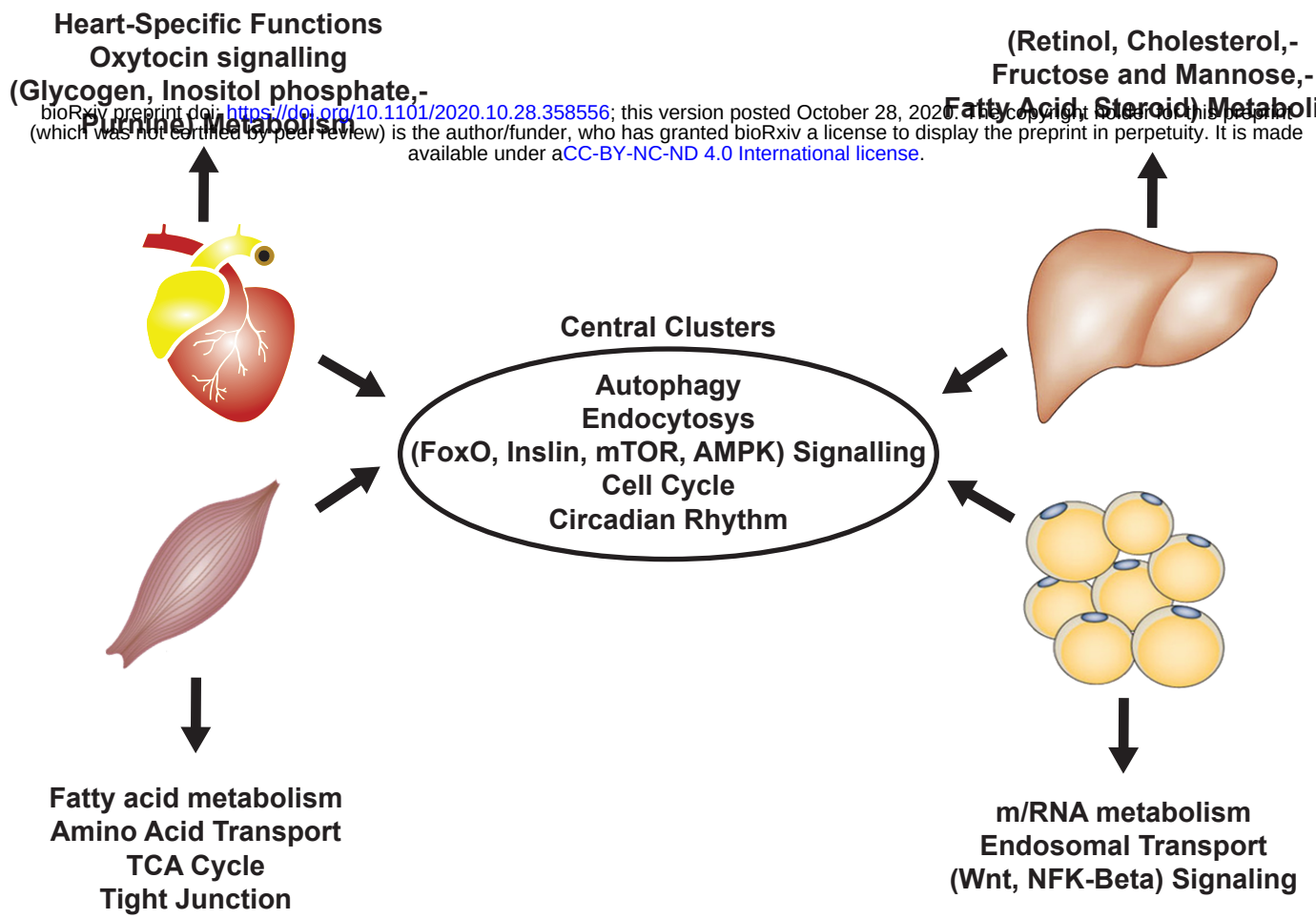

B

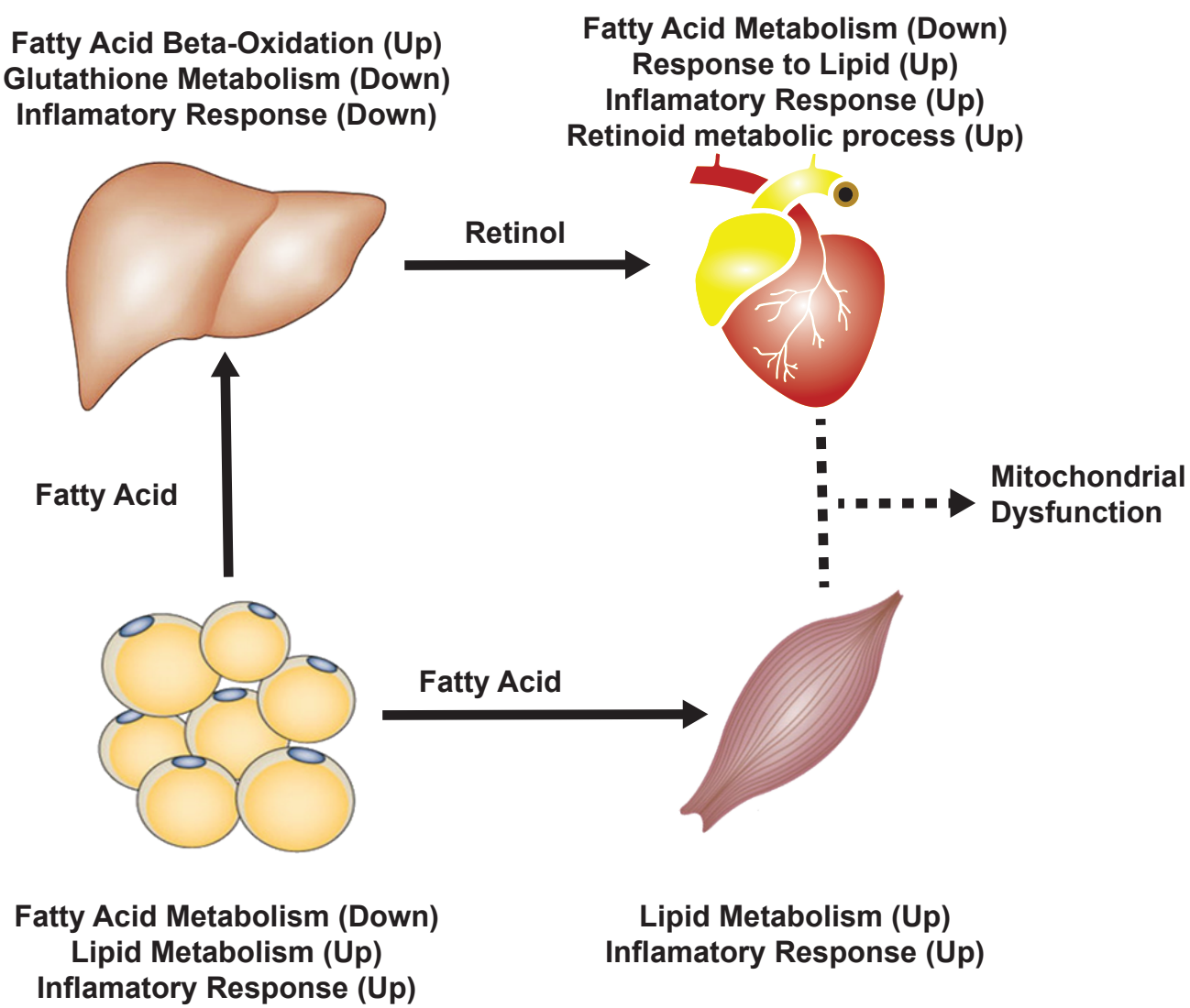

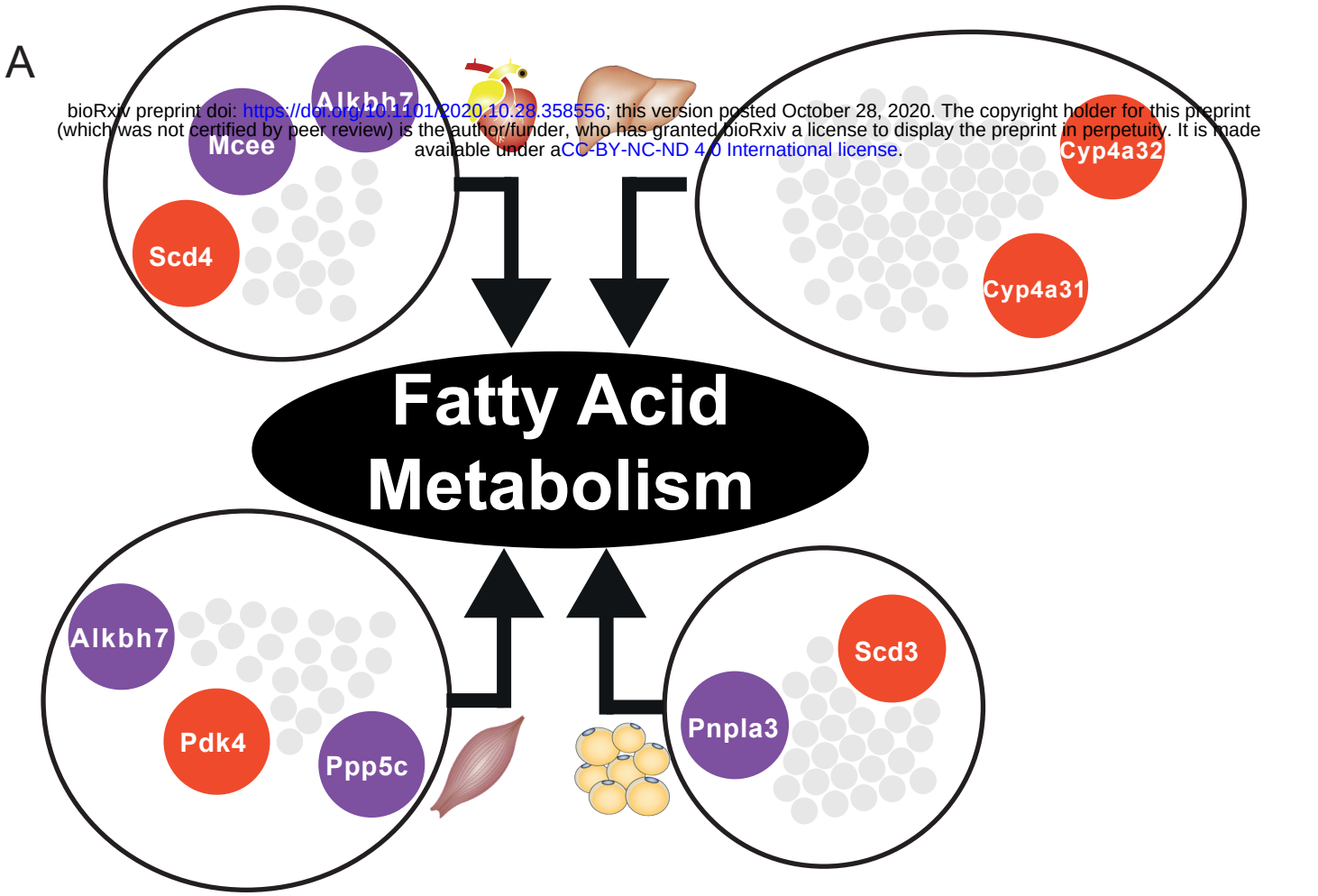

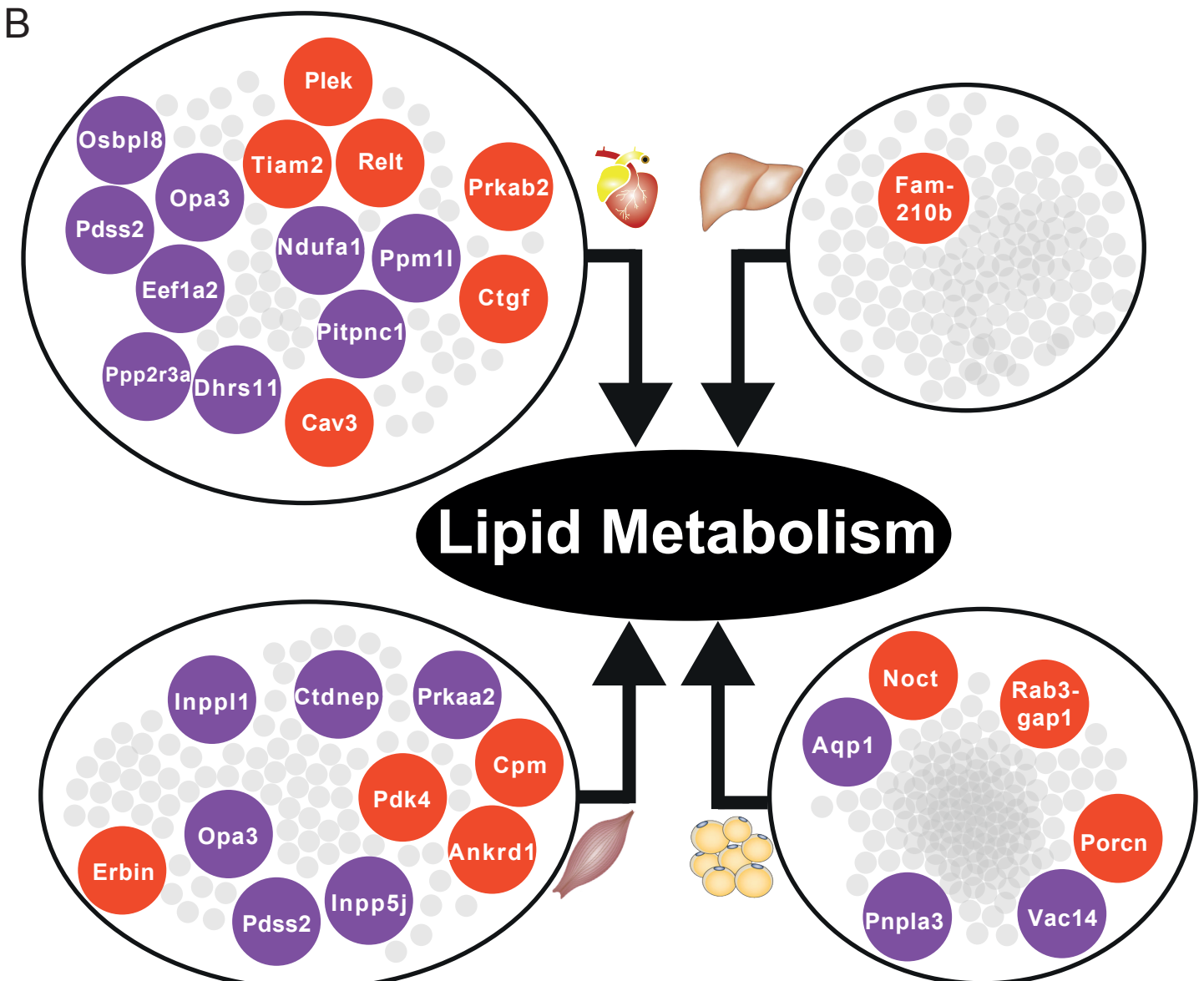

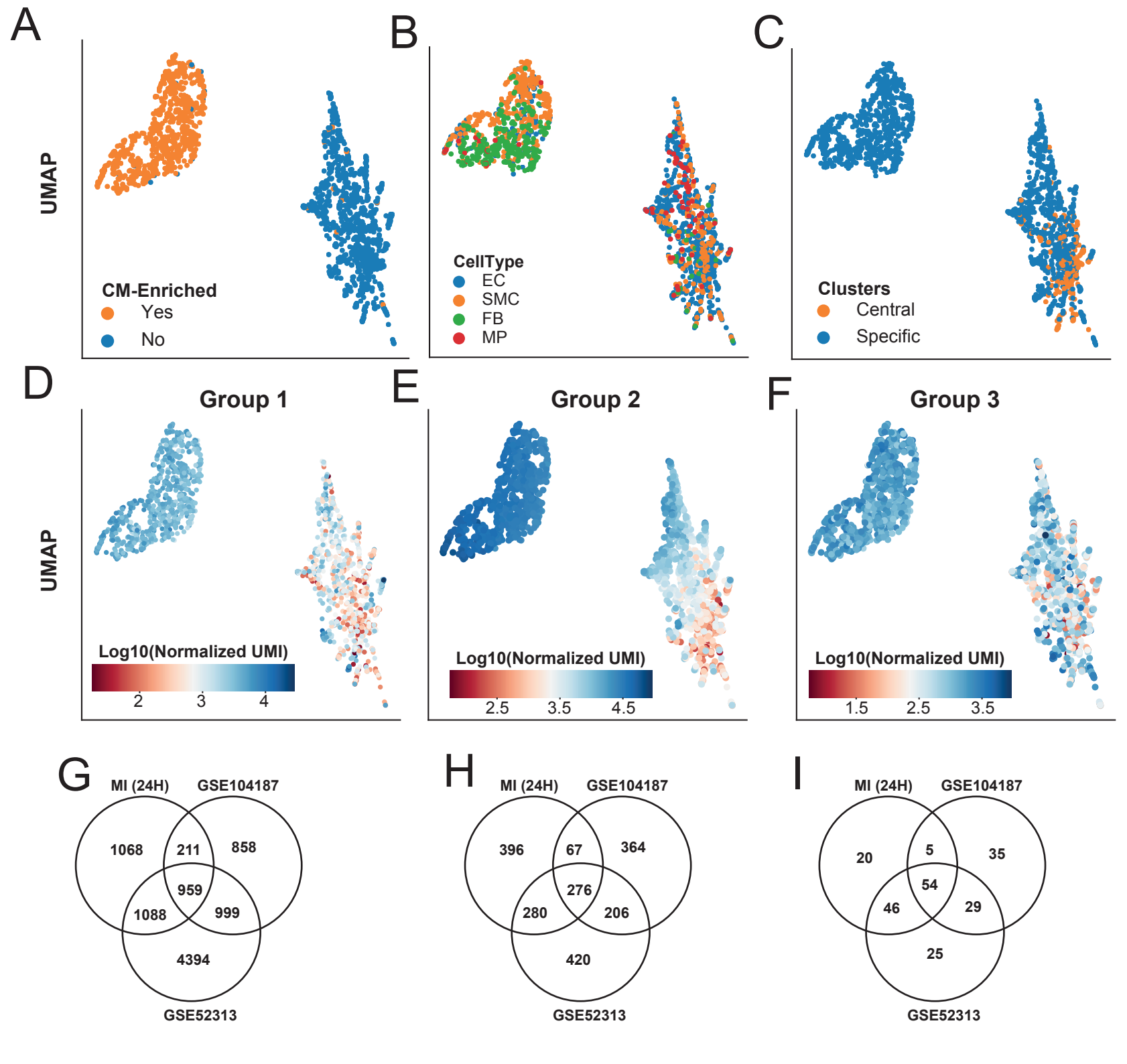
A
UMAP
CM-Enriched
Yes
No
B
CellType
EC
SMC
FB
MP
C
Clusters
Central
Specific
D
Group 1
UMAP
Log10(Normalized UMI)
2
3
4
E
Group 2
Log10(Normalized UMI)
2.5
3.5
4.5
F
Group 3
Log10(Normalized UMI)
1.5
2.5
3.5
G
MI (24H)
GSE104187
1068
211
858
959
1088
999
4394
GSE52313
H
MI (24H)
GSE104187
396
67
364
276
280
206
420
GSE52313
I
MI (24H)
GSE104187
20
5
35
54
46
29
25
GSE52313

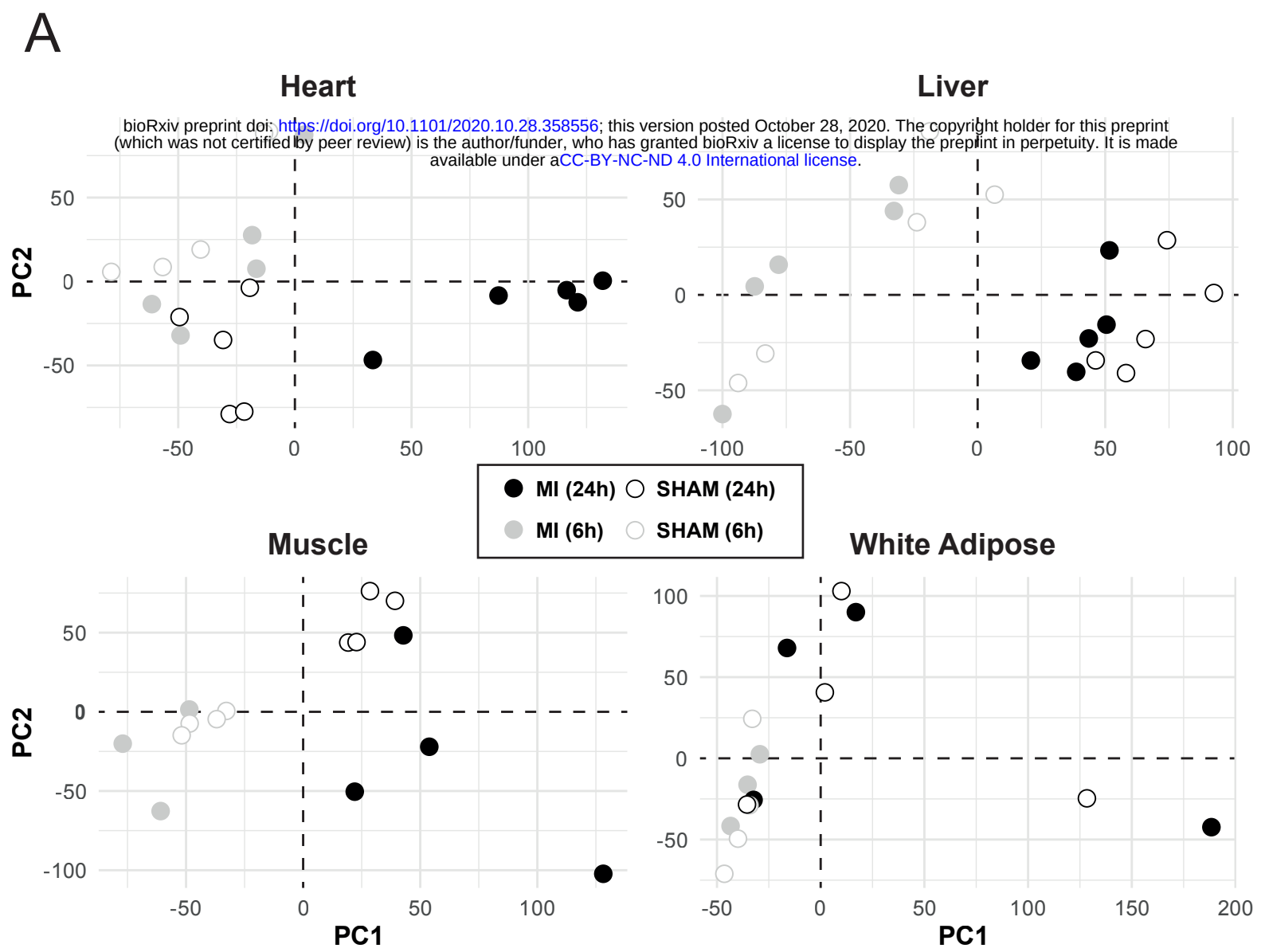

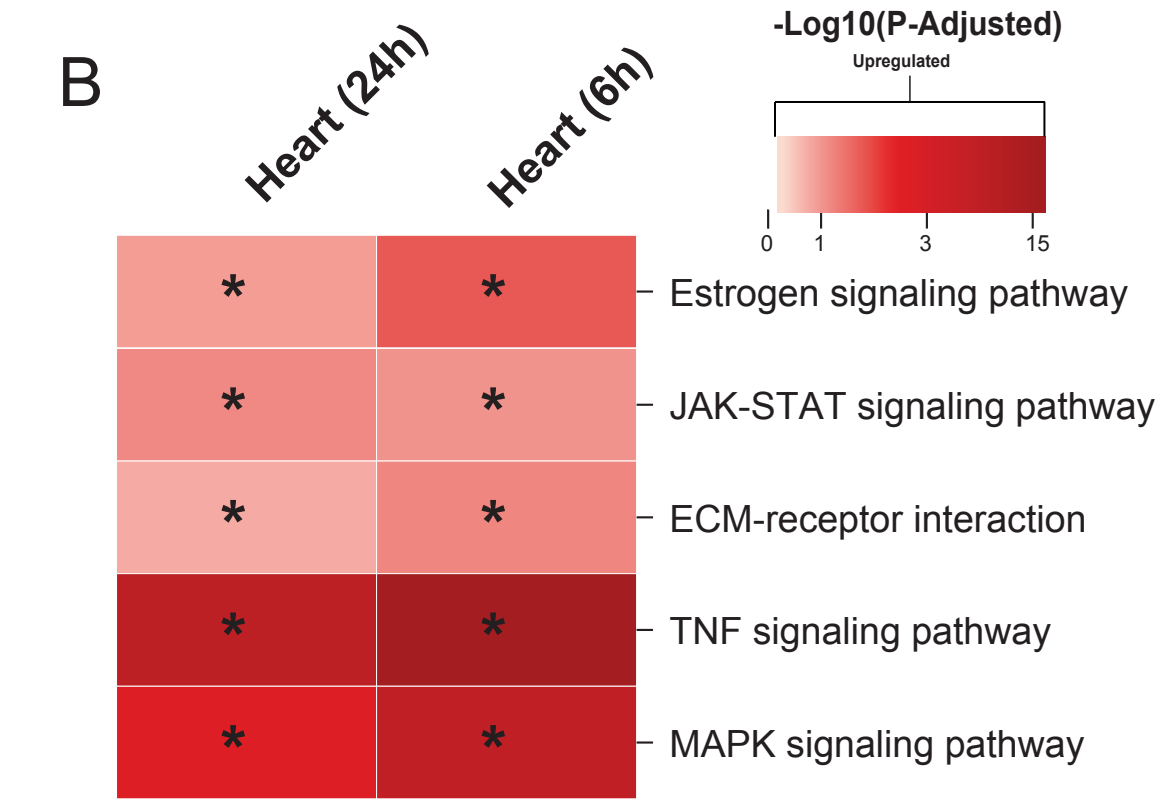

Figure S1 (A) PCA plots of each tissue showing data from mice 6 and 24 h after an MI or sham operation. The plot showed that heart was affected the most by the change in conditions and the rest were most affected by time shifts. (B) KEGG pathways related to cardiac problems show activation after an MI.

Figure S2 KEGG pathway analysis results for each tissue (A) Heart 6- and 24- hours post MI (B) Liver, Muscle, and Adipose tissue 24 hours post MI.

A

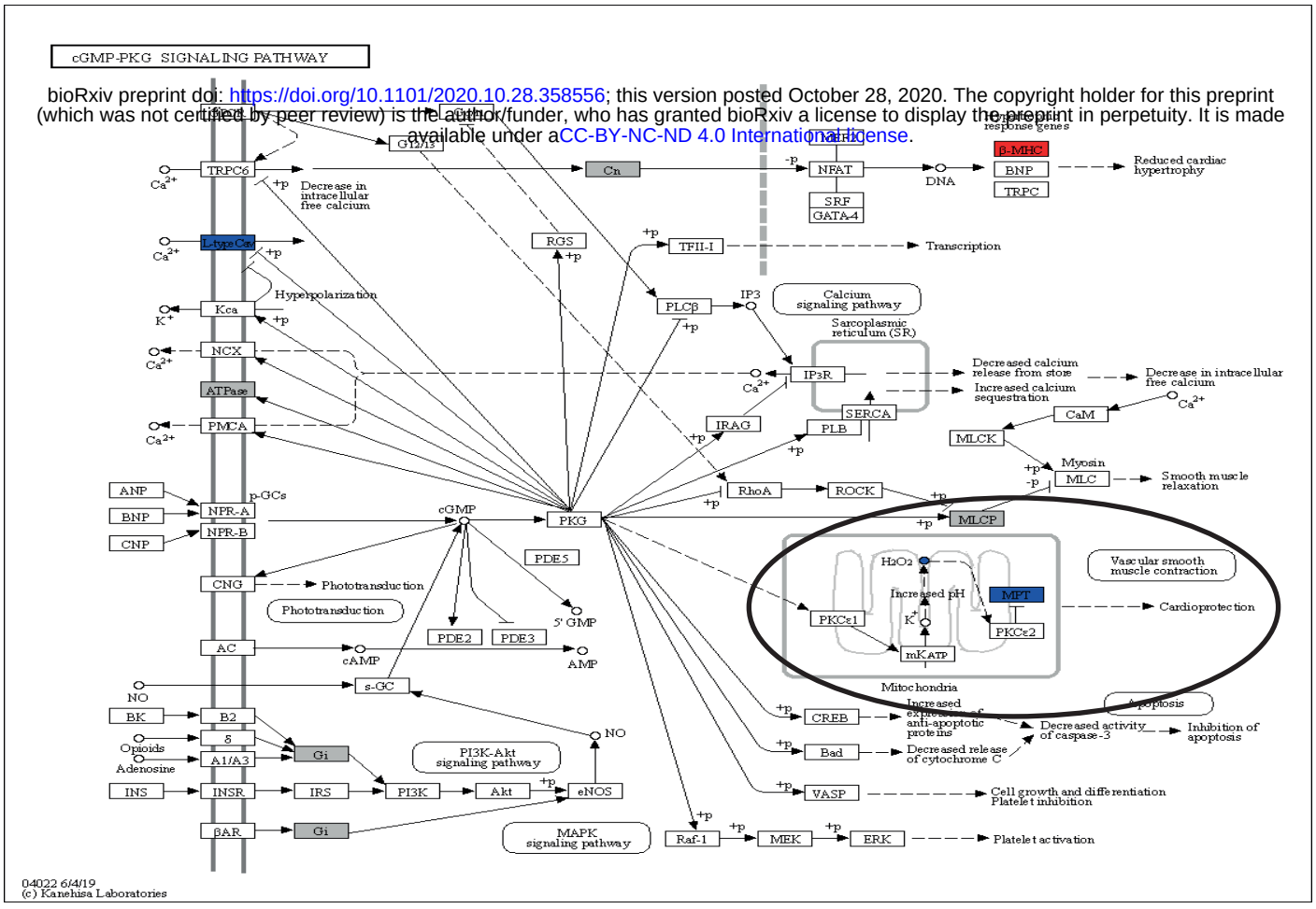

B

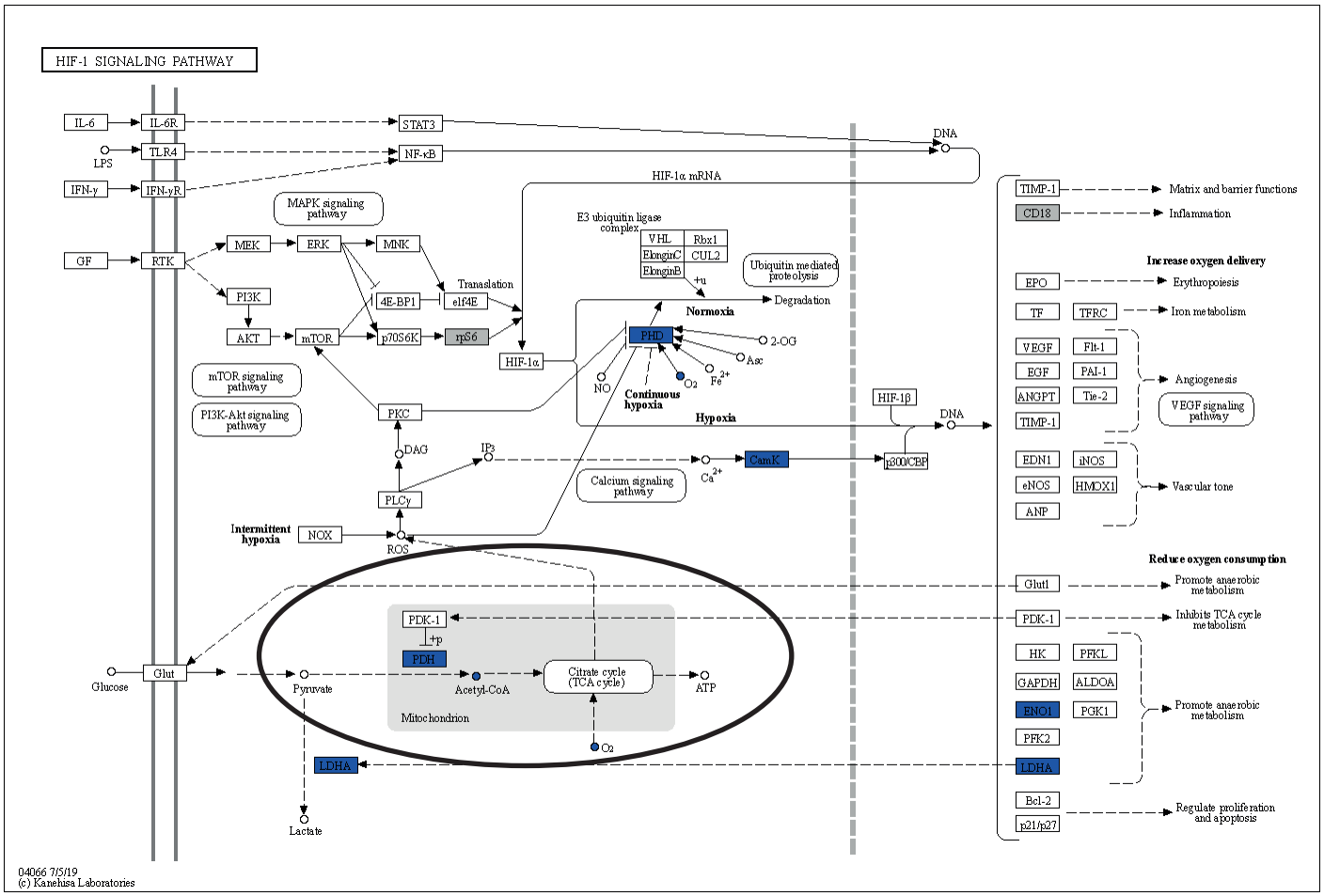

Figure S3 (A) cGMP-PKG & (B) HIF-1 signaling pathway with overlay data from differential expression and reporter metabolites analysis.

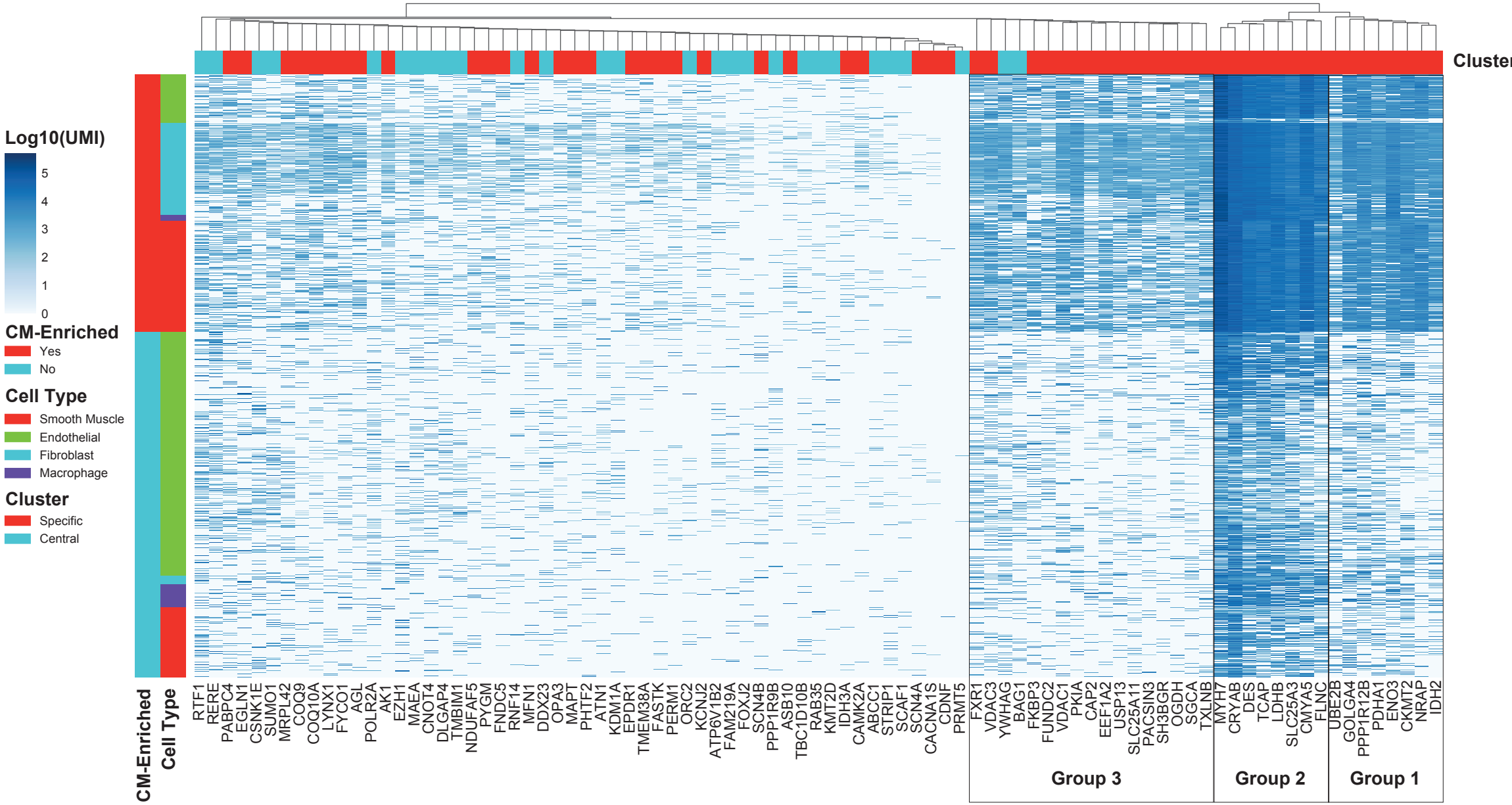

Figure S4 Expression level of central genes from most central and tissue-specific clusters and their hierarchical clustering on the single cell level.activation after an MI.

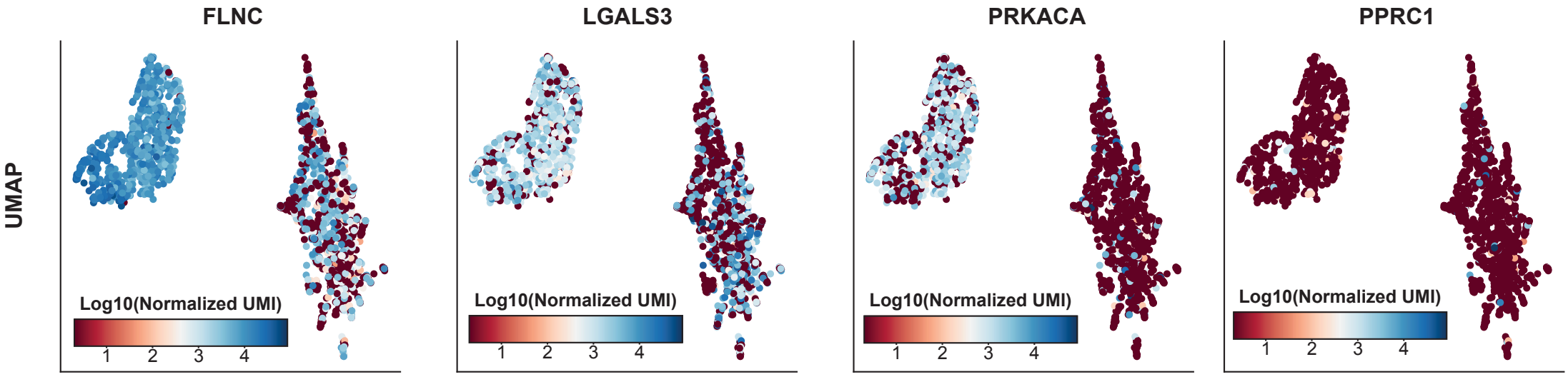

Figure S5 scRNA Expression of Flnc, Lgals3, and Prkaca.